NTNU
Norwegian University of
Science and Technology

Carbon Nanocones as Electrode Material in Lithium Ion Batteries

Marius Uv Nagell

Nanotechnology
Submission date: June 2011
Supervisor: Fride Vullum, IMTE
Co-supervisor: Morten Onsrud, IMTE

Norwegian University of Science and Technology
Department of Materials Science and Engineering

Carbon Nanocones as Electrode Material in Lithium Ion Batteries

Marius Uv Nagell

June 15, 2011

Declaration of independent work

I hereby declare that the work in this project has been performed independently and in accordance with the examination regulations of Norwegian University of Science and Technology (NTNU).

Marius Uv Nagell

Marius Uv Nagell

Preface

This master thesis is written for the masters program for nanotechnology in collaboration with the Institute of Material Science at the Norwegian University of Science and Technology. The work is mainly focused around a carbon material called carbon nanocones, which is being characterized as an anode material for lithium ion batteries. This process has been a continuation from a project which was written between August and December 2010.

The theory section 2.1 and section 2.2 have been reused from the previous project with some modifications and additions. However, the results in this work are individual and not reused from the older project. The carbon nanocones were handed to the project from n-TEC and the copper foil was given to the project by the company Circuit Foil. Separators have been provided by Celgard.

I would like to thank my supervisor Associate Professor Fride Vullum-Bruer for her help and guidance, my co-supervisor Morten Andreas Onsrud for his guidance and support in the laboratory, Anita Fossdal and Carl Erik Lie Foss for help during the experiments and writing.

Appreciated support have been given from Celgard for their free separator samples, Circuit Foil for delivering free copper foils, and n-TEC for their carbon nanocones.

Abstract

A carbon powder containing carbon nanocones was used as an anode material in lithium ion batteries. The powder was also treated in different ways, chemically, with microwaves, and with heat. The carbon powder was tape casted onto copper before being assembled into batteries with lithium metal as the counter electrode. The batteries were characterized by measuring the capacity during cycling. X-ray diffraction (XRD) and scanning electron microscopy (SEM) was used to characterize the powders and casts. Fourier transformed infrared spectroscopy (FTIR) was done to both the carbon powder and the used anode material.

The solid electrolyte interface (SEI) was characterized and found to contain components like $(CH_2OCO_2Li)_2$, Li_2CO_3, and $ROCO_2Li$. These are in accordance with what would be expected from results in the literature. SEM was used to find surface orientation of the basal and edge planes, and XRD was used to find the crystallinity.

These results showed that more graphitized powders were better with emphasis on irreversible capacity. The treated carbon nanocone powders had higher capacity than the graphitized ones, but also higher irreversible capacity.

Contents

Chapter 1

Introduction

The modern society is showing an increasing demands of portable products and therefore also better ways of storing energy. One solution is to improve the battery technology. Figure 1.1 show that lithium ion batteries have high energy density compared to other battery technologies. The possibility of making smaller and lighter batteries is important for the electronic industry as well as for the car industry.

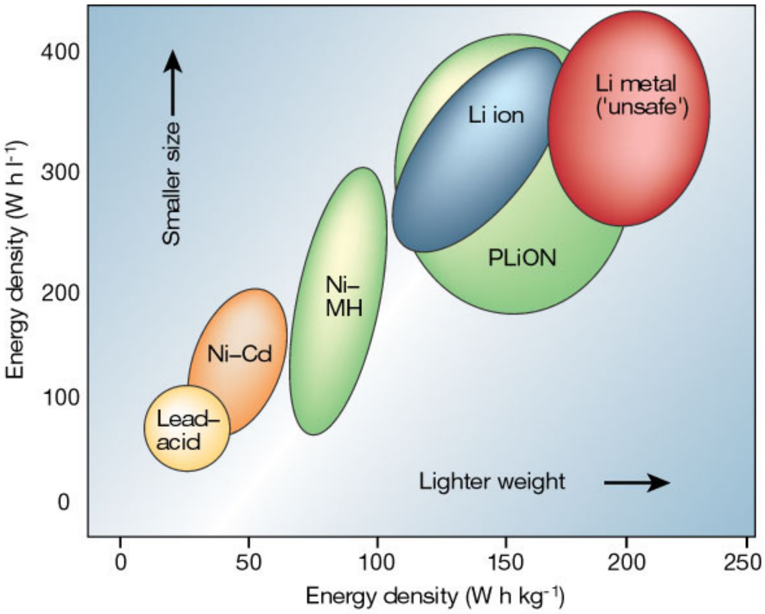

Figure 1.1: Comparison of battery technologies with emphasis on energy density [1].

Already in the 1970s lithium metal was used as anode material in batteries. These batteries had high energy densities, as shown in Figure 1.1. There were concerns though. Lithium metal is highly reactive and this gives safety issues which needs to be taken care of. The principles of the early lithium ion batteries and the commercial available batteries of today are small [2]. However research have made better electrodes and safer electrolytes which gives improved capacity, longer cycling life-time and all over safer batteries.

There have been incidents with commercial batteries where the batteries have caused dangerous situations due to the hazardous battery materials. In some cases batteries can create so much heat that a thermal runaway is reached. This again can create an explosion[3]. This is not a common matter, but it is an important aspect of lithium ion battery research.

Modern lithium ion batteries have partially solved some of the safety issues, but still there are more challenges. These batteries are rechargeable due to a reversible intercalation process which is going on between the electrodes of the battery. Cycling the battery over and over will cause the materials to become exhausted due to the volume change of the lithium ions. The structures will change during these processes and eventually create permanent deformation and similar defects. These deformations will increase and the capacity of the battery will decrease. Better and more stable structures are important to withstand the possible destructive effects of volume change [4].

Commercial lithium ion batteries are mostly using carbon as the anode material. For the intercalation process carbon has a theoretical capacity of 372 mAh/g [2] which corresponds to the stoichiometric limit of lithium ions intercalated in graphitic carbon, LiC_6. There are a lot of research groups focusing on creating better carbon electrodes. Different types of carbon are used in the search of improving the capacity. Everything from kish carbon and carbon derivatives from sugars to buckyballs and carbon nanotubes have been tested with varied results. The theoretical limit has been breached, but there might be reasons to believe that the physical limit is approaching. This gives rise to research on other materials than carbon, both carbon-metal composites and silicon are popular, but none of these have been commercialized yet.

There are still interesting carbon materials to be investigated as potential anode materials. One is carbon nanocones. This is a relatively novel material which consists of conic graphene layers covered in amorphous carbon. In 1994 the first observation of conic carbon was made [5]. Later on, in 1995, a substantial amount of carbon cone powder was discovered [6] in a batch from Kværner's carbon black and hydrogen process [7]. The powder from this batch was characterized as anode material in lithium ion batteries. It showed high initial capacity, but also high irreversible capacity [8]. The goal of this project was to investigate possibilities of improving the material's properties with treating its surface or structure. Surface and electrochemical characterization of the treated and untreated powders was also performed.

Chapter 2

Theory

2.1 Lithium ion batteries

2.1.1 Lithium ion battery principles and requirements

The basic principle of lithium ion batteries is that lithium ions go back and forth between electrodes, as shown in Figure 2.1, through an electrolyte. This is also the reason for its alternative name, rocking chair batteries [2]. When a battery is charged the ions move from the cathode to the anode, and when it is discharged the opposite occurs. Intercalation is the process where small ions are inserted into the host material, and becomes a stable part of a structure. Deintercalation is the reversed process. Intercalation processes are taking place in lithium ion batteries. These processes are accompanied by a reduction or oxidation reaction which should be highly reversible to sustain good cycle ability for a great amount of charge/discharge cycles [9, 10]. These processes will induce a volume change as ions go in and out of the original structure. Volume changes will over time deteriorate the electrode structures. Reducing these small volume changes are therefore an important target for developing electrode materials. The most common strategies used to reduce the volume changes are development of different alloys, doped, or undoped ceramic materials, or nanostructures.

Lithium ion batteries are being used in different consumer products, ranging from mobile phones and portable computers to power tools and electric vehicles. This means that different batteries need different properties. Mainly the need for high amounts of cycles as well as a good capacity are the most important requirements. The number of cycles depends on the anode and cathode materials fatigue rate and the electrolyte that is degenerated during the electrochemical processes. As the intercalation and deintercalation processes continue, the materials experience a continuous volume change. Unfortunately, not all of the lithium ions intercalate and deintercalate. They can also take part in side reactions on the electrodes. This will mean that the number of lithium ions available for further cycling is decreased, which is directly linked to the battery

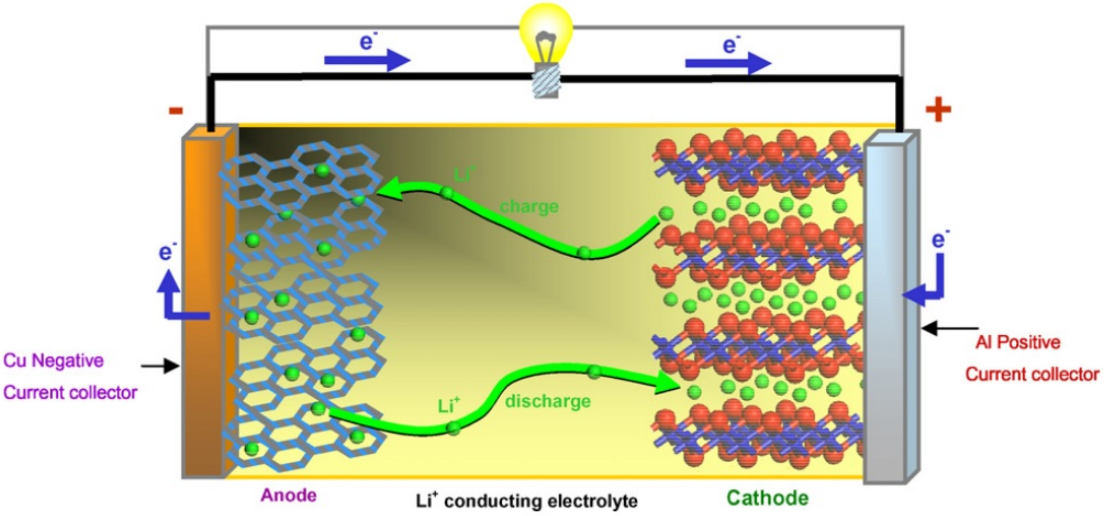

Figure 2.1: An overview of the intercalation process in a lithium ion battery.

capacity.

Battery capacity is defined as the electrical energy content or the amount of current a battery has delivered when completely discharged after one hour (Ah) [11]. In the literature gravimetric capacity is a more common capacity measurement. Gravimetric capacity is the mass specific capacity and is given in ampere hours per gram (Ah/g) [12]. Another measured capacity is volumetric capacity. This is the volume specific capacity, ampere hours per liters (Ah/l). Higher mass specific capacity gives lighter batteries and higher volumetric capacity gives possibilities of smaller batteries, see Figure 1.1. Looking at the energy content is also useful. This is given in either specific energy (gravimetric energy density) or energy density (volumetric density). They are measured in watt hours per kilogram (Wh/kg) and liters (Wh/l), respectively. To get high gravimetric and volumetric energy density it is important to have high gravimetric capacity as well as high charge density. This means that there has to be a high number of charge carriers per mass and volume unit [10]. These are criteria which separate a good battery material from a less good one. Measuring this can be done by applying charge/discharge cycles on the batteries. Another factor that plays an important role of the energy densities is the high potential between the anode and cathode.

For each charge and discharge there will be a charge capacity and discharge capacity measured. The difference in charge capacity and discharge capacity is called irreversible capacity [13]. This is an indicator of how much of the lithium ions that have been used in irreversible processes like the formation of solid electrolyte interfaces and other side reactions. The Columbic efficiency, also known as Faraday efficiency, is the ratio between the discharge and charge capacity [14]. It is a good indicator of loss in capacity, hence a good battery has to have a good Columbic efficiency for every charge/discharge.

The number of cycles the battery handle is also possible to measure. It is more commonly called lifetime. Testing the lifetime may take a long time as a good lifetime would consist of a great number of cycles. This can be shortened with numeric calculations of the trend of loss and Columbic efficiency. Having a mobile telephone battery which uses 5 days on a cycle and has a lifetime of 1000 cycles, would be nice, but is not necessary because the mobile phone would probably not withstand 13 years of use. This indicates that the lifetime of a battery is of different importance for different applications. Some applications would benefit from long discharge times (like car batteries) and some from high amount of cycles (like a electric drill).

Batteries with $LiCoO_2$, $LiNiO_2$, and $LiMn_2O_4$ cathodes and carbon anodes have shown a lifetime of 300 cycles, and potentials of about 4 V [15]. This is good for consumer electronics, but for electric vehicles, batteries with longer lifetimes are needed. Lifetimes of over 8000 cycles has been proposed as requirement. A $LiFePO_4$ cathode and anatase TiO_2/graphene composite anode gave a 1.48 V discharge voltage battery which lasted for over 700 cycles with a Columbic efficiency of around 100% the whole time [16].This indicates that it could continue with further cycling. Another promising result has been given by $LiFePO_4$/$Li_4Ti_5O_{12}$ combination cell, which is claimed to manage 15 years of use [15]. This would be equivalent to over 10000 cycles if charged twice a day. $LiFePO_4$ and $Li_4Ti_5O_{12}$ are considered having large potential for making long lasting batteries, especially for electric vehicles. $LiFePO_4$ has already been chosen by light electric vehicle users in areas where low temperature performance is not required [17]. In this project there has been no lifetime testing or long term cycling.

2.1.2 Anodes

The anode is the electrode that receives the lithium ions upon charging. These materials have to be able to intercalate a great amount of lithium ions into their structure and deintercalate efficiently upon discharge. On the battery market today, most lithium ion batteries have anodes consisting of different types of carbons. Researchers are constantly trying to enhance the anodes using new forms of carbon by making different structures, alloying carbon with other materials, and trying out new materials. Another material of special interest is silicon. Both of these are being further described here.

Carbon

Carbon is the most commonly used anode material. The stoichiometric limit of intercalated lithium ions in graphitic carbon is six carbon atoms per lithium ion, LiC_6 which is shown in Figure 2.2. This yields a theoretical capacity of 372 mAh/g [2], but could be overcome by changing the stoichiometry.

Carbon based anodes is preferred because compared to many other alternatives, carbon experiences little volume change upon intercalation and deintercalation. Graphite only increases with 9.4% in volume when lithiated to LiC_6 [2]. Perfect graphitic structures can reach the theoretical limit, but amorphous carbons are thought to have higher potential lithium uptakes than the stoichiometric limitation of LiC_6 [18]. Therefore by altering the micro and nano structures of carbon particles, the capacity can be increased. Artificial graphite was developed by optimizing particle and pore size in the material [19]. Anodes made by this material showed a specific capacity of 360 mAh/g with 95% Columbic efficiency, and it could sustain high discharge rates.

Modified natural carbon and artificial carbon exhibit great potential for reaching specific capacities above the theoretical maximum. Air oxidation of natural graphites has improved the electrochemical characteristics and kish carbon show intercalation capacities above 372 mAh/g [20]. Many other varieties of carbon have been tried too, like carbon nanotubes (CNTs).

Tin filled CNTs has been investigated as anode material, and showed promising results with specific capacities above 700 mAh/g for 40 cycles [21]. The problem with this material is the high irreversible capacity and the high cost which make them less attractive for commercial use. Another way of using CNTs is to align them on a substrate. This does not remove the high irreversible capacity which the CNT has, but one test showed a stable discharge capacity of 265 mAh/g over 50 cycles [22].

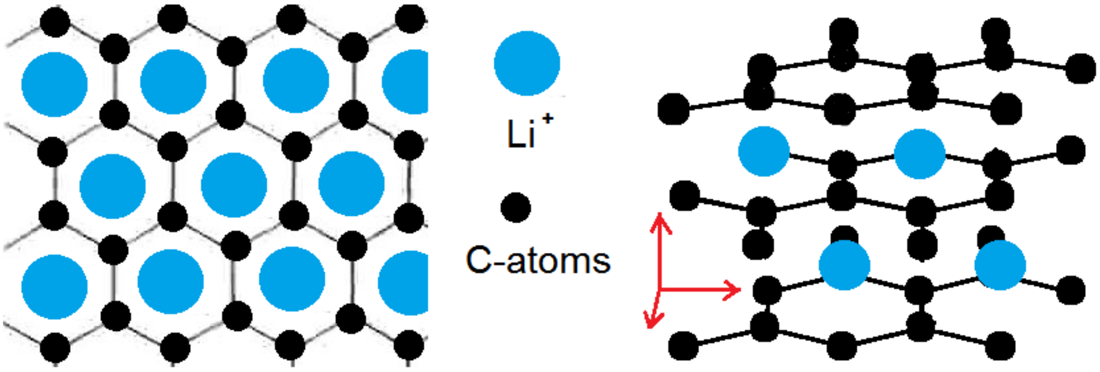

Figure 2.2: This is a schematic of the LiC_6 structure, in the basal plane view to the left and from an angeled, edge plane view to the right.

Silicon

Silicon is an opponent to the carbon based anodes. Silicon has a theoretical capacity which has been reported to be around 4200 mAh/g [2, 9], and greatly exceeds the values of carbon. This corresponds to a stoichiometry of Si_5Li_{22}. The problem of this material is the volume change it experiences during intercalation and deintercalation. The volume change is observed to be between 300-400% [2, 9]. This volume change makes the silicon to crack up and deteriorate. As an alternative to replace carbon as anode material, silicon research needs to focus on eliminating the expansion problem, but without losing too much of its potential capacity. This is the primary problem of silicon anodes and has been the biggest hindrance for commercialization.

Solutions to the volume expansion would be to give room to the expanding volume by creating different nanostructures. Quantum dots have been used as an alternative. Coated with amorphous carbon these particles were used and resulted in a first charge capacity of 1257 mAh/g [23].

One research group tested the potential of a silica-carbon composite [24]. This gave a reversible capacity of around 710 mAh/g for 100 cycles, which is a very good result. In an attempt to overcome the silicon's volume expansion a group made silicon nanowires [25]. For 20 cycles the capacity of the batteries were around 3500 mAh/g which is an exceptionally high capacity.

2.1.3 Cathodes

The cathodes are materials which should deintercalate lithium ions upon charging. This gives a high demand to structure stability of the material, as well as low energy barrier for deintercalation. There are three common types of anodes used in lithium ion batteries; layered lithium-metal oxides, lithium-manganese spinels, and polyanionic compounds, usually called olivines.

2.1.4 Electrolytes

Electrolytes for lithium ion batteries are mediums containing lithium ions and which allows for transport of these ions between the electrodes. It is therefore an essential component for the battery to work. There are many approaches to making an electrolyte. The standard method is to solve a lithium based salt in a solvent which do not contain water. The solvents can vary from simple liquid solvents, to solvents held in place in porous membranes, or even polymers. Polymer electrolytes are not as common as solution based electrolytes. They are more attractive, though, because they are nonflammable [2, 26]. Electrolytes can also be lithium conductive solids.

One of the most common electrolytes is $LiPF_6$ dissolved in ethylene carbonate (EC) and dimethyl or diethyl carbonate (DMC and DEC, respectively). This is, as a lot of other electrolytes, a compromise between advantages and disadvantages. It is flammable and only electrochemically stable up to 4.5 V [2], but it is not explosive such as $LiClO_4$ or as poisonous as $LiAsF_6$. $LiPF_6$ can also be decomposed to HF, which can be a problem if the batteries overheat and explode or leak [27]. Implementation of manganese based cathodes, as earlier mentioned, would demand removal of $LiPF_6$-based electrolytes. The reason for this is that they do not work very well together, because of the HF created. This is an example of the fact the use of electrolyte should be adapted to the electrodes used.

2.1.5 Solid electrolyte interfaces

During the first charge/discharge cycle of the lithium ion battery, there will be some decomposition of the electrolyte into inorganic species like Li_2CO_3, Li_2O, LiCl and organic polymeric species like R-OLi, R-OCO_2Li and $(CH_2OCO_2Li)_2$ (R is a hydrocarbon chain) [28, 29, 30]. These components, together with other species depending on the system, will deposit on the electrode surface and form a solid electrolyte interface (SEI) [28, 31]. This happens on carbon anodes as well as other electrode material. The irreversible capacity of electrode materials is partially caused by the SEI formation.

Wang *et al.* [32] observed that lithium ions can intercalate into carbon nanospheres at the defect sites of the edge planes. These defect sites are again also responsible for the SEI formation. For porous carbon materials the high surface area will create excessive side reactions with the electrolyte and form SEI to inhibit reversible faradaic reactions. This will give a larger irreversible capacity loss in the first cycle and also give a poor cyclic stability. As anode material can consist of small, nanosized carbon particles, this will also affect the surface area, which again can increase the irreversible capacity [33]. The stability of the SEI is also critical for the effective utilization of carbon [34], as well as for effective use of any carbon. This is because a stable SEI would prevent continuous decomposition of electrolyte, meaning that the SEI thickness will stay constant and prevent further increase in irreversible capacity as well as rapid declines in performance. The formation mechanics of the SEI is different for the basal plane and edge formation. Control of the exposed area of the two mechanism sites could enhance and stabilize the SEI. An idea to reduce the SEI formation and keep a fast intercalation/deintercalation speed is to use crystalline domain size of around 45 *nm*, which would be intercalated in about 0.2 *ms* [35]. Creating these graphite particles with radially aligned crystallites would have very little disorder in the structure which would reduce the formation of SEI. SEI formation can be minimized, but will always be present to some degree.

The SEI is not only a problem. This layer protects the electrodes from other decomposition reactions that can occur. Controlling the SEI formation is important. Too thick SEI will create a high resistance film and lithium ions will not be able to easily intercalate in the carbon anode. To control the SEI the surface reactions and properties need to be characterized. This project will try to characterize the SEI formation on anodes made of carbon nanocones and investigate ways of modifying the surface to see what effects this will have on SEI formation.

2.2 Carbon nanocones as anode materials

2.2.1 Carbon materials

Carbon can exist as different structures, such as diamond, graphite, fullerenes, graphene, carbon nanotubes, and carbon nanocones [4]. The latter is the least known and comes from Kværner's carbon black and hydrogen process [7]. Carbon nanocones is the material investigated in this project.

Diamond is formed under high pressure and temperatures. The diamond is a very hard and mechanically stable material and is used in everything from jewelry to drill bits. Graphite on the other hand, is used in pencils and as electrodes for different electrochemical applications. This is also a crystalline material, but does not exhibit the same properties as diamond. It is highly electrical conductive in the plane direction, whereas diamond is an electrical insulator in all directions. On the other hand, diamond is a relatively good thermal conductor. Graphite is also very soft compared to the hardness of diamond.

Carbon nanotubes [36] and fullerenes [37] are two other materials, found much later (1991 and 1985, respectively) than diamond and graphite. The carbon nanotubes (CNTs) are small tubes which have proven to be far stronger that steel [38] and can be either semiconducting or conducting [39]. They can have single or multiple walls and have a lot of possible applications, ranging from capacitors to reinforcement in composites. Fullerenes on the other hand, are a family of ball shaped molecules consisting of carbon pentagonal and hexagonal rings. The smallest stable, and most common, fullerene is the C_{60}, but structures as C_{70}, C_{84} and C_{100} are found too. They are thought to be used as everything from containers for small ions to superconducting materials in structures with alkali metals (A_3C_{60}, A - alkali metal) [40].

Graphene is a single sheet of hexagonally honeycomb structured carbon, while graphite is blocks of layered graphene. Graphene was first isolated and characterized in 2004 [41], and has been shown to be a versatile, strong, conductive, and transparent film. This gives raise to different uses like a transparent conductor [42].

Carbon nanocones, which are the focus of the current work, were first observed by Klaus Sattler and Maohui Ge from the University of Hawaii in 1994 [5]. They observed nanocones of sizes up to 24 *nm* in length and 8 *nm* in diameter of the cone opening. They made the nanocones with vapor condensation of carbon on a graphite substrate and later did scanning tunneling microscopy (STM) studies of their product. Applications have not been reported, but several research groups have investigated basic properties of the carbon nanocones.

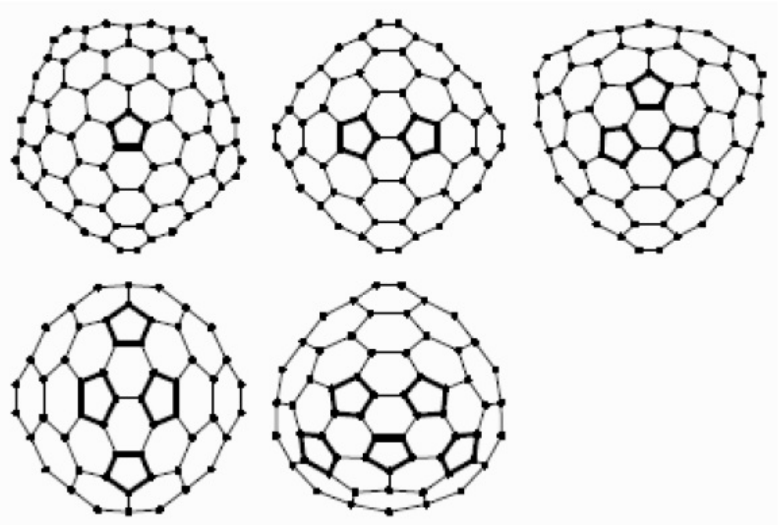

Figure 2.3: The five defects that make carbon cones [43].

Carbon nanocones

The carbon material from Kværner's Carbon Black and Hydrogen Process [43] is a material which consists of cones, disks, and impurities of carbon black. The discs make up around 70% [44] of the powder, whereas the angled nanocones make up about 20% [44] of the powder. The rest is impurities of carbon black [44]. Carbon nanocones have five different angles, depending on how many defects there are in the apex of the cone. The mentioned defects are missing carbon atoms in the apex, as shown in Figure 2.3, which creates one or more pentagons in the graphene sheet and forces the sheet to bend into a cone. The more defects the smaller angle of the cone, which is given by the following relation:

$$\sin(\frac{\phi}{2}) = \frac{2\pi - p \cdot \frac{\pi}{3}}{2\pi} \tag{2.1}$$

Where ϕ is the possible angles and p is the number of defects ranging from 0 (flat discs) to 5 which gives an angle of 19.2° [45]. This restriction in number of cone angles rises from the geometry and limitations of the honeycomb structure of the sheets that bend. If more defects are introduced it would simply not be an open cone. The nanocones are not only single cones, but layers of cones with wall thickness of 20 *nm* to 50 *nm* and opening diameters roughly between 0.8 μm up to 3 μm [43]. The outside layer of the cones consist of amorphous carbon. SEM images of carbon nanocones can be seen in Figure 2.4.

Application of the carbon nanocones has not been reported to a great extent. It has been investigated as a potential thermal rectifier material by Yang *et al.* [46]. As carbon nanocones consists of both amorphous and crystalline carbon it should be highly possible for the cones and discs to be used in lithium ion batteries.

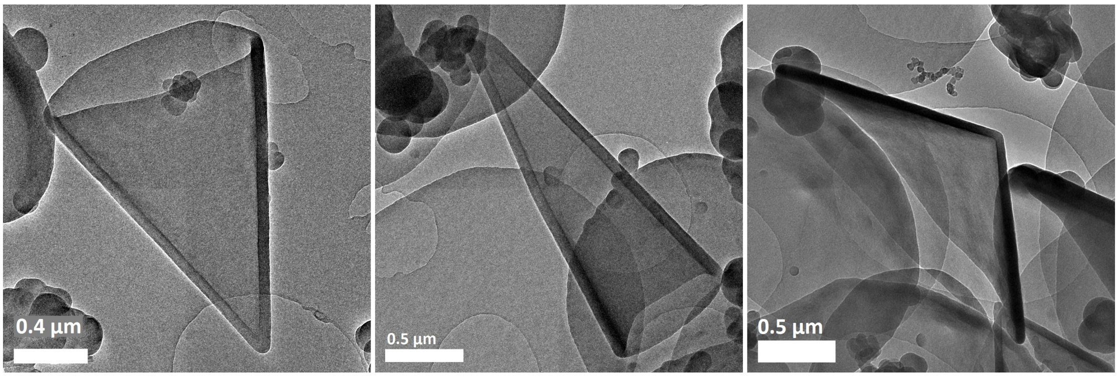

Figure 2.4: Three different sized cones with 4 (left), 5 (middle), and 1 (right) defects. [Images: Morten Onsrud].

2.2.2 Slurry processing

Producing carbon nanocone anodes is not does not consist of just adding the carbon nanocone powder to a current collector and assemble this into a battery. The powder needs to be mixed into a slurry which can be controlled and further be casted on the current collector material. The current collector is a thin copper film.

Mixing the slurry properly is important. Consistent slurry mixing will make sure that the casted film thickness is controllable.

The thickness is important as it can alter the internal pressure of the battery, which will affect the battery performance. Another reason to control the thickness is the amount of active material used. If the anode film is too thick, the material near the current collector will not be used. Too thin anode film and the maximum potential for the anode is not being used. This makes it important to control the thickness to be sure that the right amount of active material is used. This has been done during an earlier experiment [8], and the methods that were used there are being used in this project as well.

2.2.3 Binder

The anode usually consists of carbon. Carbon itself will not automatically stick to the current collector. Therefore a binder material is needed to keep a good contact between the carbon and the metal current collector. The binder also gives the electrodes enhanced mechanical strength. An ordinary anode is composed of 90-95 wt% carbon which is held together by 5-10 wt% of a polymeric binder.

A problem with the binder material, is that it has a negative effect on the electrochemical characteristics of the anode and cathode [47]. Choosing an appropriate binder is therefore important. Polyvinylidene fluoride (PVDF) is a commonly used binder for carbon materials. The reason for using this polymer is that it provides chemical stability, reversibility, chemical resistance, and good wettability, as well as being inexpensive [48].

2.2.4 Safety issues

Preventing thermal runaway or chemical breakdown during use of the battery should be an important target in battery research. Lithium is a reactive metal and reacts violently in an oxygen atmosphere or when exposed to water [27]. Usually the failure of the lithium ion batteries are caused by short circuits inside the battery, as well as exposure to high temperatures or overheating during charging and discharging [49, 50]. Leakage of electrolyte and exposure to water are also sources to dangerous failure mechanisms. Reasons for internal short circuiting could be deposition of lithium dendrites on the carbon anode which penetrate the separator [49]. Another reason could be contaminations of metals in the electrolyte which could start other unwanted reactions or just short circuiting of the system [50].

Electrolytes

The electrolyte solvents used in lithium ion batteries today have low boiling points and flash points around 30°C. Replacing these with low- or non-flammable electrolytes is an important step towards safer lithium ion batteries. This would prevent the risk of explosion and thermal runaway [2].

The batteries today use electrolytes which have a tradeoff between cell performance and flammability. The flammability can be reduced by using additives, but in most cases it will affect some of the performance as well. Fluorinated and organo-phosphorus compounds are amongst the most investigated additives [2, 51]. The flame-retardant trimethyl phosphate has been studied as an additive as it is chemically stable on both the cathode and the anode side in lithium ion batteries [51].

Separators

In a battery the electrodes must never be in contact with each other. If they do, the battery will short circuit and become destroyed. To prevent this from happening, separators are used. These are porous films which allow for ions and electrolyte to flow around on each side, but at the same time prevent contact between the electrodes. Separators have to be thin films so they do not take up any extra space or increase the internal resistance in the battery . Neither can they react with the electrolyte, anode, or cathode.

Porous polymer films are often used as separators, as they are usually inert and easy to produce [52].

2.2.5 Recent development

There are numerous reports on different anode materials, especially carbon anode materials. None of them mention carbon nanocones, but their results can be used to indicate whether the results of this project are satisfying. Yoo *et al.* tried out different versions of a type of modified graphene. This was graphene nanosheets combined with carbon nanotubes or fullerenes [53]. The carbon nanotubes and fullerene combinations, as well as the pure form of graphene nanosheets, all had gravimetric capacities above the theoretical value. 730, 784, and 540 mAh/g, respectively. After 20 cycles the values decreased to 480, 600, and 290 mAh/g, respectively. Wu *et al.* [54] investigated the capacity of hard carbon, which is said to not have more than about 250 mAh/g capacity. Their result for hard carbon was a capacity of 252 mAh/g. Wt *et al.* had also doped hard carbon with boron oxide, B_2O_3, and found out that 15.3 wt% was the optimal amount. This composition gave a capacity of 394 mAh/g. This is barely above the theoretical value for carbon, 372 mAh/g, and several other reports have exceeded this value. Su *et al.* did not exceed the theoretical capacity with their hollow carbon shells [55]. They tried to dope their carbon shells with nitrogen as well, but achieved the same results, 325 mAh/g, after both 1 cycle and 100 cycles. This shows good stability of the material. Su *et al.* concluded that the higher the crystallinity of the carbon anode, the higher the electrical conductivity, and therefore it could be thought that higher crystallinity would give better cycle ability at higher currents. Y. Wang *et al.* tried to make carbon anodes of carbon nanospheres of diameters less than 100 nm with nitrogen-functional groups prepared by carbonizing polypyrrole nanospheres [32]. These spheres showed an initial capacity of 420 mAh/g and after 60 cycles showed a capacity loss of 0.15% per cycle. Q. Wang *et al.* used hard carbon spheres with mesopores. The spherule size was in the range of 6.5 μm. These spheres gave a reversible capacity of 430 mAh/g, and by modifying the spheres surface by dispersing it with 100 nm particles of SnSb the capacity was increased to 480 mAh/g. Khomenko *et al.* [56] investigated a variety of different carbon and carbon/silicon composite materials, which gave the results in Figure 2.5.

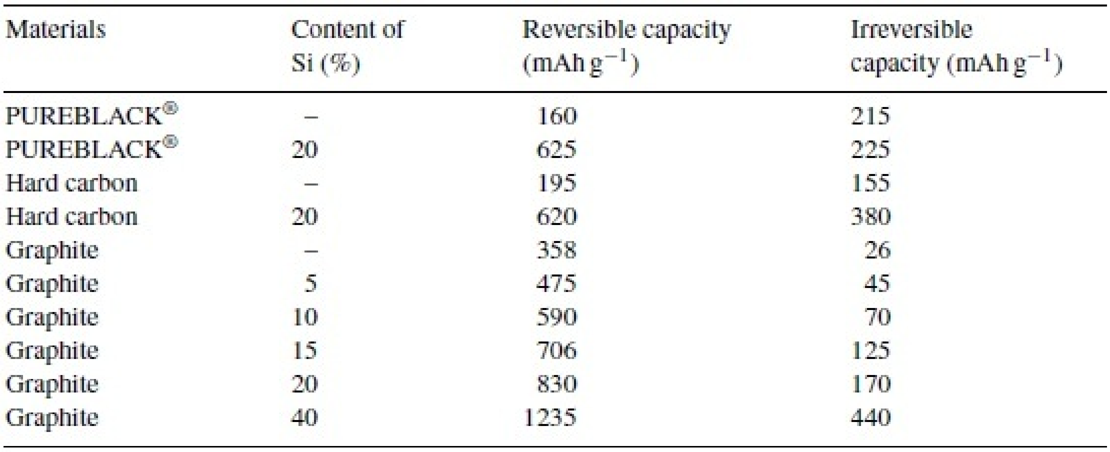

Materials	Content of Si (%)	Reversible capacity (mAh g^{-1})	Irreversible capacity (mAh g^{-1})
PUREBLACK®	–	160	215
PUREBLACK®	20	625	225
Hard carbon	–	195	155
Hard carbon	20	620	380
Graphite	–	358	26
Graphite	5	475	45
Graphite	10	590	70
Graphite	15	706	125
Graphite	20	830	170
Graphite	40	1235	440

Figure 2.5: A table from Khomenko *et al.* which shows the capacity and irreversible capacity of different carbon materials [56].

2.3 Characterization

2.3.1 Infrared spectroscopy

Infrared spectroscopy (IR) is a characterization technique using infrared radiation (wavelength, $\lambda \sim 1\,mm - 1\,\mu m$) [57] to characterize the surface of a material. Materials exposed to the infrared radiation absorbs different energies, dependent on the atomic bonds of its molecules. IR spectroscopy uses the absorption of the radiation to determine what kind of bonds that are present. The molecule's absorption of energy disrupts the equilibrium state of vibrational and rotational energy and the molecules exitaion energy increases.

This technique has the advantage of being relatively cheap, as it does not need ultra high vacuum and have a good variety of different ways of using optical phenomenons to optimize the characterization of different materials [**?**]Verma20106332). There are also limitations and disadvantages with the IR. For instance, the beam which usually cannot characterize a very large areas, is limited to the characterization possibilities for large inhomogeneous surfaces [29].

Fundamentals

IR spectroscopy utilizes infrared light, which is obtained from lasers. These laser beams are electromagnetic radiation which have characteristic wavelengths. A normal representation of the specific wavelengths is wavenumber, the reciprocal of the wavelength. It also relates to the frequency of the light wave and the speed of light:

$$\tilde{\nu} = \frac{1}{\lambda}[cm^{-1}] = \frac{\nu}{c}[cm^{-1}] \tag{2.2}$$

where $\tilde{\nu}$ is the wavenumber, λ is the wavelength, ν is the frequency of the light wave and c is the speed of light [57].

Molecules consist of atoms which maintains certain distances between each other. These distances between the atoms relates to the interactions between electrons in the outermost orbits, and gives rise to vibrational and rotational energy states [57]. Through simple physical models these energies can be calculated. The vibrational energy relates to the model of a diatomic molecule of a harmonic oscillator, which can be simplified to a mass on a spring connected to a wall. This model gives the frequency of the vibrating diatom as:

$$\nu = \frac{\pi}{2}\sqrt{\frac{k}{\mu}},\ \mu = \frac{m_1 m_2}{m_1 + m_2} \tag{2.3}$$

where k is the spring constant between the diatom masses, μ is the reduced mass of the diatoms two atom masses, m_1 and m_2 [57]. As this is a classical model, and the reality is not classical, the system needs to be looked at by solving of the one-dimensional Schrödinger equation which is given by:

$$-\frac{h}{4\pi m}\frac{d^2\psi}{dx^2} + V(x)\psi = E\psi \tag{2.4}$$

where h is Planck's constant, m is the mass of the atom, Ψ is the eigenfunction of the system, $V(x)$ is the potential field i the x-direction, E is the energy for the system [57]. Solving this equations gives the following result for the discrete energies of the system:

$$E_v = h\nu(v + 0.5), where\ v = 0, 1, 2, ... \tag{2.5}$$

where ν is the oscillator frequency from the classical model, v is the vibrational quantum number and is characterizing the ground state of the system [57]. Implementing Equation 2.5 to a diatomic model gives the following relation between two energy states, the starting state and the excited state:

$$E' - E'' = h \cdot \nu = h \cdot \tilde{\nu} \cdot c \Rightarrow \tilde{\nu} = \frac{E' - E''}{h \cdot c} \tag{2.6}$$

where E'' is the energy state of the particular atomic group before excitation and E' is a energy state with a higher quantum number [57]. This gives a relation between the energy and vibration for the diatomic molecule. Quantum physics makes the steps discrete. Discrete steps gives discrete energies which can be absorbed, and the same is true for the rotational energies. Using this theoretical knowledge gives the possibilities of making models and calculating what kind of different bonds in different molecules absorbs different wavelength radiations. Implementing this with experimental results gives the possibilities of characterizing materials using IR radiation.

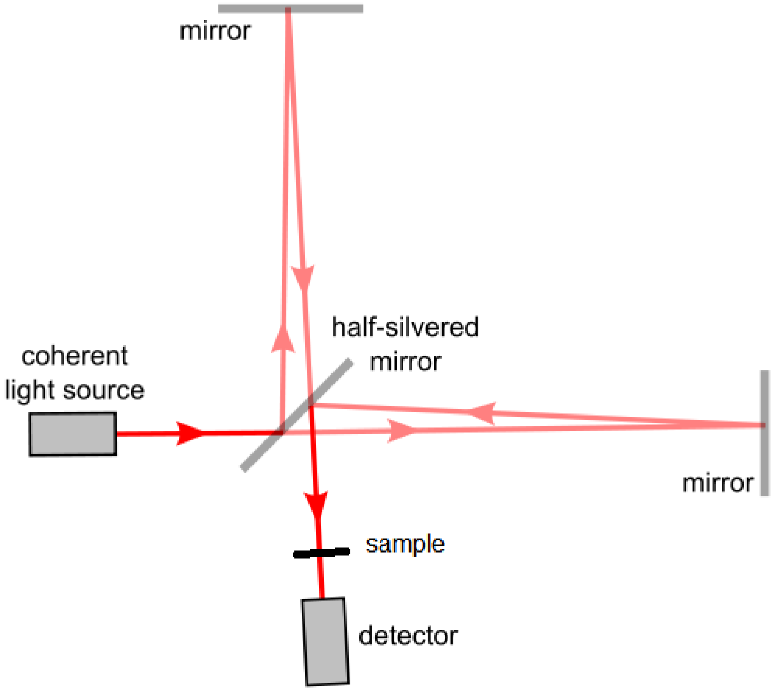

Figure 2.6: A schematic [58] of a Michelson Interferometer, which is a beam splitter used in Fourier transformed IR spectrometers.

The original use of prisms to create the IR radiation was limited to wavelengths around 2-15 μm [57]. Using a Fourier transform (FT) technique the entire range of IR radiation could be used. The Fourier transformed IR (FTIR) technique uses a beam splitter and two mirrors to make interference in the incident light at the sample. A normal way of doing this is to use a Michelson interferometer, shown in Figure 2.6. The signals for each wavelength that arrive at the detector can then be presented as:

$$I(x) = I_0 + I_0 cos 2\pi\tilde{\nu}x \tag{2.7}$$

where $I(x)$ is the detected intensity of the IR radiation and I_0 is a initial intensity, x is the difference between the path length of the two split beams, and $\tilde{\nu}$ is the wavenumber of the light [57]. The cosine signal creates an interference pattern if the radiation source contains several wavelengths. This final signal that the detector receives is an addition of all the single frequencies. This pattern is then converted to a spectrum by using a Fourier transform on Equation 2.7:

$$S(\tilde{\nu}) = \int_{-\infty}^{\infty} I(x) cos 2\pi\tilde{\nu}x \, \mathrm{d}x \tag{2.8}$$

where $S(\tilde{v})$ is the signal strength as a function of wavenumber $\tilde{v}$ [57]. This signal is what gives the represented FTIR spectra.

Not all the absorption is detectable. There are possibilities of IR-inactive modes of vibration. These inactive modes are due to vibrations that cancel each other out, causing no visible absorption. Another phenomenon is frequency overtones which make interference with similar frequencies and can take energy from other vibrations states. This can enhance another frequencies, making it more visible than the others. Binary combination bands are another phenomena that can make IR spectroscopy hard to interpret. These bands are combination of two or more frequencies which appears as visible signals in the IR spectra. Binary combination bands are not belonging to any specific bonds, but are just the signal addition of combined bands [57].

Characterization with IR spectroscopies has been done on a lot of materials. This gives great knowledge of different materials absorption spectra, which makes it easier to analyze new materials and compare similar materials to get more precise analysis. In this project FTIR is used to find differences on the differently treated carbon nanocone surfaces. There are also done analyses of anode material that has been cycled.

SEI characterization

FTIR is a suitable tool for characterizing SEI, especially because it does not need ultra high vacuum [29]. Research groups have used IR spectroscopy in combination with other techniques like X-ray photoelectron spectroscopy (XPS) and Raman spectroscopy [29, 59, 60, 61]. This comparison of different techniques can differ FTIR peaks which are made from groups present on the sample and those that are created from combination peaks and overtones [59]. Many research groups have been using a lot of resources on trying to identify specific groups on carbon [62, 63], oxidized carbon [60, 61, 63, 64, 65, 66, 67] and the SEI layer on carbon anodes [29, 68].

Published literature is a helpful supplement when it comes to interpreting FTIR results. Verma *et al.* gathered a great amount of SEI data and have given an overview of the most common products of the SEI formation [29]. Table 2.1 shows the different species and their reported vibration absorption values. This will be an important resource in the analysis of the FTIR data which is done in this project.

2.3.2 X-ray Diffraction

X-ray diffraction (XRD) uses X-rays to measure distance between planar layers in a crystal lattice. The incident X-ray beam is reflected off of crystal lattice planes. By changing the incident X-ray beams angle to the material which is being characterized, signal peaks will appear for different crystal planes. These reflection peaks can be calculated from knowing the lattice parameters of the sample. This is known as Bragg's law:

Component	Functional group	Vibration (cm^{-1})
$(CH_2OCO_2Li)_2$	C=O asym st	1634 [69], 1650 [70], 1654 [71]
	CH_2 bend	1396 [69], 1400-1450 [70, 71]
	C=O sym st	1300 [69], 1301 [71], 1320-1290 [70]
	C-O st	1050 [69], 1100-1070 [70], 1083 [71]
	OCO_2 bend	822 [71], 840-820 [70]
$ROCO_2Li$	C-H	2950-2820 [72], 2930-2850 [70]
	C=O asym st	1610 [73], 1650 [70, 73, 74], 1668 [71], 1685 [75], 1680-1640 [72]
	CH_2 bend	1450-1400 [70, 72]
	C=O sym st	1300 [73], 1350 [75], 1350-1300 [72], 1350-1320 [70, 74]
	C-O st	1060-1020 [76], 1090 [73], 1100 [72], 1115 and 1044 [75], 1100-1050 [74], 1100-1080 [70]
	CO3 bend	820 [72, 74, 74], 855 [75], 840-820 [70]
Li_2CO_3	C-O st	1400 [77], 1470-1450 [74], 1450 and 1500 [71], 1510-1450 [73], 1520-1480 [70], 1520-1500 [74], 1542-1455 [75]
	${CO_3}^{2-}$ bend	875 [70], 876 [75], 879 [71], 890-870 [73]
ROLi	C-H st	2963 [73], 2900-2700 [74]
	C-O st	1000 [73], 1050 [78], 1080 [73], 1100-1000 [74]
	Li-O st	600-500 [74]
Li_2O	Li-O st	600 [73, 74]
RCOOLi	C=O asym st	1500-1700 [77]
LiOH	O-H st	3670 [77], 3675 [74], 3660-3675 [75]
$Li_2C_2O_4$	C=O st	1640 [77]
HCOOLi	C=O st	1606 [69], 1620 [79]
	COO^- bend	1380, 790 [69, 79]
PVDF (as binder, not SEI)	C-F st	1200 [73]

Table 2.1: Verma *et al.* [29] gathered the following data from the literature. Abbreviations: asym - assymetrical, sym - symmetrical, st - stretching, bend - bending

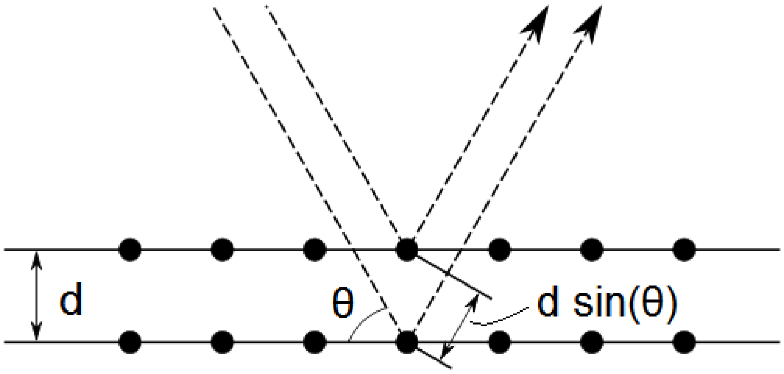

Figure 2.7: A schematic [80] of an incident X-ray beam being reflected off a crystal lattice plane, which is described by Bragg's law (Equation 2.9)

$$n\lambda = 2dsin\theta \tag{2.9}$$

where n is a integer (1, 2, 3,$\cdots$) representing the order of reflection, λ is the wavelength of the X-ray, d is the spacing between two lattice planes, as shown in Figure 2.7, and θ is the angle of the incident beam [81].

Amorphous samples will have randomly oriented planes in all kinds of directions, and will therefore give out distorted signals which is not possible to use. The more crystalline the material is, the sharper and stronger the signals will become. [81]

2.3.3 Charge/discharge characterization

To electrochemically characterize batteries for many cycles with controlled parameters a potentiostat can be used [82]. This can be done with ordinary batteries or other test cells. All test cells are being put under one or many cycles where the current or voltage are either controlled or measured. Many cycles can be performed to measure the cycle life and capacity of the materials that are being tested.

The most common way is to test a half-cell. For lithium ion batteries this would imply using lithium metal as an electrode in the test cell. For a half-cell, the lithium metal would work as the anode and the carbon material would become the cathode. This is because the lithium ions in the battery have a lower potential when they are intercalated in the carbon material compared to the lithium metal.

The characterization process consists of charge and discharge cycles. Limits of either voltages or currents are set for each cycle. Everything from long term projects to a single charge or discharge can be done, depending on the goal of the characterization. In this project there has been no long term characterization. This project is interested in the SEI formation and irreversible capacity.

The data that are extracted from these types of characterization are the materials capacities. These can be described as the amount of lithium ions that can be intercalated or deintercalated in the material. An important parameter is the total amount of lithium ions that can be stored per mass unit (mAh/g), called initial capacity. Another important factor is the irreversible capacity, the amount of lithium ions that are either trapped in the material or used in the formation of the SEI. The irreversible capacity can indicate how much of the lithium that is being used. In an ordinary lithium ion battery, the cathode will have to use some of its limited supply of lithium ions in these processes. In the test cell, this is not a issue as the lithium electrode has immensive supplies of lithium ions. Another problem is the capacity loss for each cycle which is due to the degeneration on the electrodes. This is an important factor for a battery's lifetime.

Chapter 3

Experimental

3.1 Equipment

- Ball mills - RETSCH PM 100 (planetary mill) and RETSCH MM2200
- Glove Box - MBRAUN LABmaster SP
- Scanning Electron Microscopy (SEM) - Zeiss SUPRA 55 VP FESEM and Hitachi S-3400N
- Tape caster - RK K Control Coater Model 101
- X-Ray Diffraction (XRD) - Bruker D8Focus, with solid state LynxEye detector
- Cell test system - Solartron Analytical 1480 MultiStat
- Fourier Transformed Infrared Spectroscopy (FTIR) - Bruker IFS 66v
- Surface Absorption measuring (BET) - Tristar 3000 Surface Area and Porosity Analyzer with a VacPrep 069 Sample Degas System
- Tube furnace
- Microwave - Matsui MS-106WH

3.2 Chemicals and materials

The chemicals and materials used in this project can be found in Table 3.1.

Table 3.1: The chemicals and materials used

Chemical/Material	Formula	Manufacturer
Carbon nanocones	C	n-TEC
Heat treated carbon nanocones, 2700°C for 3hrs in Ar	C	n-TEC
Heat treated carbon nanocones, 1800°C for 3hrs in Ar	C	n-TEC
Functionalized carbon nanocones	C and 12 *wt%* O	n-TEC
Graphite, SLP30	C	Timcal
Kynar, Polyvinylidene fluoride	$(CH_2\text{-}CF_2)_n$	Arkema
N-Methyl-2-pyrrolidone	C_5H_9NO	Aldrich
Lithium hexafluorophosphate	$LiPF_6$	Aldrich
Diethyl carbonate	$C_5H_{10}O_3$	Aldrich
Ethylene carbonate	$C_3H_4O_3$	Aldrich
Layered polypropylene and polyethylene	$(CH_2\text{-}C[CH_3]H)_n/(CH_2\text{-}CH_2)_n$	Celgard
Copper	Cu	Circuit Foil
Lithium	Li	Alfa Aeser
Hydrogen peroxide, 30%	H_2O_2	Sigma-Aldrich
Nitric acid, 65%	HNO_3	Merck
Potassium bromide, FTIR grade (99.9%)	KBr	Sigma-Aldrich

3.3 Powder treatments

3.3.1 Microwave treatment

The untreated carbon nanocones were exposed to microwaves in a Teflon container. The container could be sealed, which made it possible to treat the powder in argon atmosphere. Air atmosphere was also used. The parallels made are named MWCCAr and MWCCAir. MWCCAir was the only parallel to be tested in a half-cell. All microwave treatments used 1150 W. It was the maximum power of the microwave oven, which was a commercial microwave oven modified with a ventilation pipe. The duration of each treatment was 20 seconds.

3.3.2 Heat treatment

Two samples of carbon nanocones were heat treated at 2700 and 1800°C in argon atmosphere for three hours. They were treated and delivered from n-TEC and named HTCC2700 and HTCC1800, respectively. The untreated carbon nanocones (CCRAW) and oxygen-functionalized carbon nanocones (CCO12) from n-TEC were also heat treated at 950 and 900°C, respectively, for one hour in argon atmosphere. They were named HTCC950 and HTCC900Ar/CCO12. The name CCO12 refers to the oxygen content of 12 % in the carbon nanocones. Heat treating this powder was a way of trying to remove most of the oxygen from the CCO12 powder.

3.3.3 Oxidation treatment

The heat treated powders were also chemically treated. 3 grams of HTCC950 was put in a beaker and stirred together with 200 *ml* nitric acid or hydrogen peroxide with a magnet stirrer for 4 hours. For the nitric acid the mixture was heated to 50°C. The hydrogen peroxide mixture was not heated at all.

After 4 hours the the mixture was filtrated with filter paper. The powder was also rinsed with distilled water until the pH of the rinsing water was the same before and after the rinsing. Then the powders were dried in an oven at 150°C for 24 hours.

The powders that were wet chemically treated with nitric acid and hydrogen peroxide are called CCHNO3 and CCH2O2.

The CCRAW and HTCC2700 were oxidized at 900°C in air and called CC900Air and CC900Air/2700, respectively. CC900Air was also heat treated at 900°C in argon atmosphere. This powder was called HTCC900Ar/Air, and again the reason for this treatment was to remove oxygen on the from the powder.

3.4 Slurry mixing

Slurry no.	Carbon type	Carbon mass [g]	PVDF mass [g]	Total NMP mass [g]
25	MWCCAir	9.50	0.50	45.27
26	HTCC2700	9.51	0.51	80.41
27	HTCC2700	*	*	*
29	HTCC950	9.50	0.50	33.00
30	CC900Air	0.9500	0.0510	3.51
31	CCH2O2	0.9516	0.0509	3.72
32	HTCC950	0.9500	0.0501	3.35
33	HTCC900Ar/Air	0.9499	0.0498	4.05
34	CC900Air/2700	0.9502	0.0498	4.61
35	HTCC900/Ox	0.9513	0.0515	3.40
36	SLP30	1.4263**	0.0757	3.00

Table 3.2: The mass composition of all the carbon nanocone slurries made. *Slurry 27 was a dilution of slurry 26, so the same weight ration of HTCC2700 and PVDF, but with more NMP. **SLP30 mass = 1.3897 g and carbon black mass = 0.0364 g.

Making anodes require a binder for the active material. This needs a solvent to make sure the mixture is thoroughly dispersed. The active material used was carbon nanocones in above mentioned forms, the binder was polyvinyldiene fluoride (PVDF) and the solvent used was N-methyl-2-pyrrolidone (NMP). The mass ratio of carbon nanocones and PVDF was 95:5. The amount of solvent used was varying with powder used. This amount varied to get slurries with viscosities that was suited for tape casting. The used amounts can bee seen in Table 3.2.

All the work with NMP was done inside a fume hood. For slurries 25, 26 and 29 the components were put directly in a 500 *ml* alumina ball mill jar. 5 alumina balls with a diameter of 30 *mm* were used for mill-mixing the components, as shown in Figure 3.1. The speed of the milling was 250 rpm and the slurries were milled until they were properly mixed. The milling time varied between 15 and 45 minutes, unless more NMP was added to the mixture. Adding of NMP would increase the milling time. Earlier results [8] indicate that longer milling times should not have an effect on the powder particles, so the main target is to get proper mixing and viscosity suited for tape casting. The viscosity was not measured, but experience from making slurries [8] made it easy to determine when the viscosity was suitable for casting.

After the ball milling was finished, the slurry was transferred to a Büchner flask, and evacuated with a water jet pump for one and a half hours. This will remove the air bubbles that have been mixed in the slurry during the ball milling.

Slurries 30 to 32 were mixed in another, smaller type of mill. This was a small steel

Figure 3.1: A slurry which is not done milling. It has not gotten the desired viscosity. [Photo: Morten Onsrud]

container with one steel ball. The steel containers could not contain as much as the previous container, so the recipe was cut down to a tenth. Scaling down the slurry dis not cause any problems.

After being put in the steel container, the mixtures were then milled with the RETSCH MM2200 for at least 6 minutes, until the mixtures were properly mixed. If the viscosity was too high, more NMP was added and the mixture was milled again. There were no need to remove air from the smaller batches.

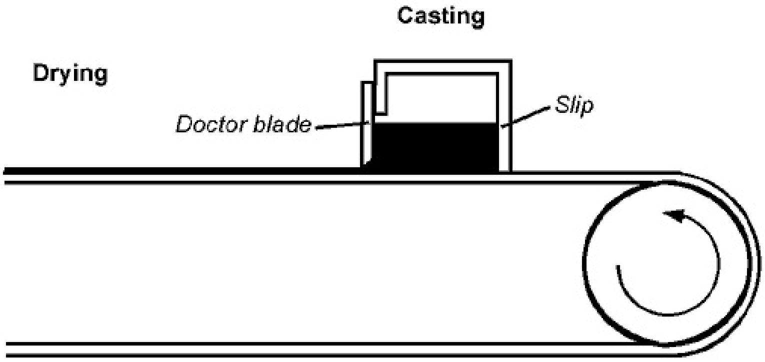

Figure 3.2: A figure which shows the principle of tape casting. Here with a doctor blade [83].

3.5 Tape casting

Tape casters use a doctor blade to make films on substrates, as illustrated in Figure 3.2. This project's tape caster used doctor blade which moves over a stationary heating plate. A plastic film was attached to the plate, and a copper film was attached to the plastic. Speed of the caster was usually set to 1, but the more viscous the slurry were, the faster speed was used. The casting velocity was usually set to 1 which corresponds to 2 m/min. The velocity could be adjusted between 2 and 15 m/min. For more viscous slurries higher velocities were used.

After the film was casted, it was dried at 60°C on a hot plate inside a fume hood for 90 minutes.

When the film was finished drying, it was put in a vacuum oven at 120°C overnight to remove remaining moisture and solvent. The thickness of the film was measured for every electrode.

3.6 SEM, XRD, BET and FTIR

SEM was used to investigate and compare the casted surface with the powders they were made of. The SEM was also used to see if any structural changes were visible, and to see what kind of planes and surfaces that was most exposed in the casts. Which surface that is is important as there are different reaction mechanisms on the different surfaces. XRD was used to characterize the different powders to get information on the differences in crystallinity and composition. BET was used to investigate the specific surface area of the different powders. FTIR was done on powders and cycled anode material to see if there were any distinct differences on the surfaces of the materials, as well as to characterize the SEI surface. This was done by mixing the material with potassium bromide and pressing pellets. Initially, this was done in air, but with drying of the powders and pellets in an vacuum oven. Later on this was done in the glove box, and the pellet was pressed inside a plastic bag to ensure that exposure to air was minimized.

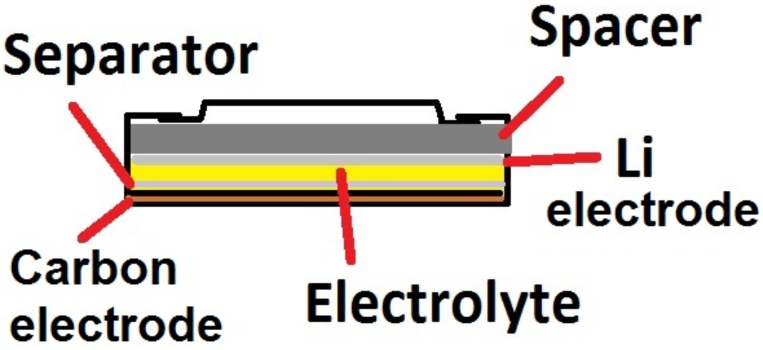

Figure 3.3: Schematic of the assembly order for the coin cells used.

3.7 Electrolyte

The electrolyte used in the batteries was 1 *M* lithium hexafluorophosphate ($LiPF_6$). The salt was added to a solution of 1:1 (%mass) ratio of ethylene carbonate (EC) and diethyl carbonate (DEC). The EC had to be heated up to above 35°C and then DEC was added while stirring with a magnet stirrer. $LiPF_6$ was added to the solution and stirred until all the salt was dissolved. The electrolyte was kept in small glass flasks with screw caps. All the work was done inside a glove box.

3.8 Battery assembly

When the tape casted carbon nanocone film was finished drying, it was moved to a glove box with an argon atmosphere. In this glove box the oxygen and water content was held below 0.1 ppm. Casts from the slurries in Table 3.2 as well as a CCRAW and a SLP30 cast which were made earlier [8], were used as electrode material in the half-cells.

The batteries assembled were CR2016 button cells, which mean that the total height of the battery was 1.6 *mm* and the diameter of the battery was 20 *mm*. Figure 3.3 shows the assembly order of the different components.

This project used lithium as a reference electrode, which makes the batteries half-cells. In regular lithium ion batteries the carbon is defined as the anode because the lithium in the carbon structure oxidizes upon discharging. In the half-cells of this project the lithium becomes the anode as upon discharging the lithium oxidizes. At the same time the lithium ions intercalate into the carbon, which is being a cathode. The batteries made in the project also have a potential when assembled, whereas ordinary lithium ion batteries would need to be charged before they get a high potential. This fact will not interfere with results, but is important to know, so that applied currents and measuring is done properly.

The labeling of the batteries were done as follows. The first part of the name refers to what kind of carbon nanocone powder that was used. The rest is different details like casting thickness or cast number, and the last number is the battery number for the cast. An example is HTCC2700-150μm-1, which is HTCC2700 battery number one from the cast which used 150 μm height on the doctor blade.

3.9 Battery characterization

The batteries were placed into a battery holder. The batteries were charged and discharged with a potentiostat. The batteries were exposed to different charging and discharging cycles, starting with a slow initial cycle process before faster cycles were initiated. As the batteries had an initial potential, the first step is a discharge process.

The following charge and discharge rates were used. The initial discharge was performed in two steps, a primary discharge rate of 10 mA/g was used to reach 0.05 V, before a last discharging step of 5 mA/g was used to reach 0.04 V. The first charge was done with a rate of 20 mA/g until 1.5 V was reached. The rest of the cycles were performed with charge and discharge rates of 40 mA/g. The charge and discharge were terminated at 0.05 and 1.5 V, respectively. The lower limit was set so that there would be no electroplating of lithium metal on the carbon electrode.

Later on a program based on different charge rates where used. First the same initial discharge/charge cycle was performed. The only difference was that for the last discharging step the potential was kept at 0.05 V until the current had dropped to 5 mA/g. Then there were two cycles of C/20, C/10, C/5, C/2 and C respectively. C represents the time needed to discharge the battery for one hour.

Chapter 4

Results

4.1 X-ray Diffraction

Figure 4.1 and Figure 4.2 shows that most of the carbon powders are highly amorphous. There are in fact no major differences in the powders except for the HTCC2700, HTCC1800, CC900Air/2700 and graphite (SLP30). HTCC1800 shows higher crystallinity than the all the powders with exception of HTCC2700, CC900Air/2700 and SLP30. There is a visible peak shift for the heat treated carbon nanocones as the heat treatment temperature increases.

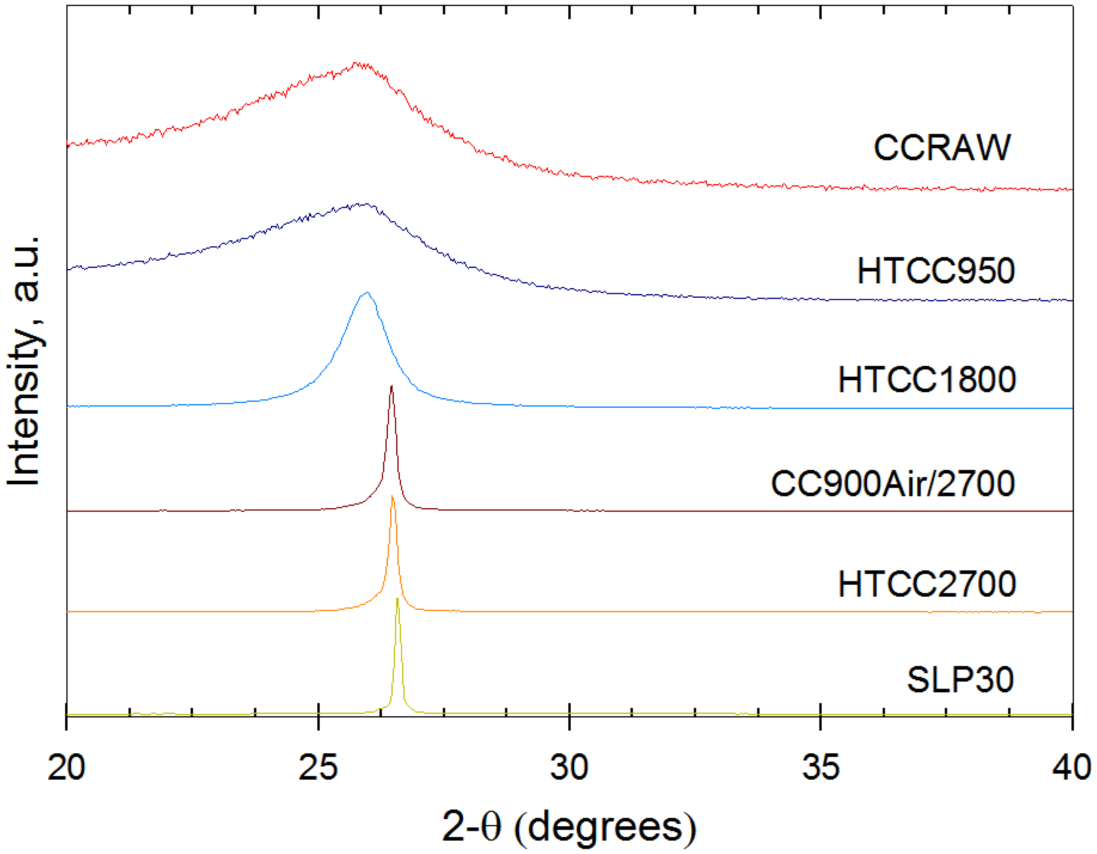

Figure 4.1: The XRD results for the heat treated carbon nanocones, as well as for commercially available graphite (SLP30) and untreated carbon nanocones (CCRAW).

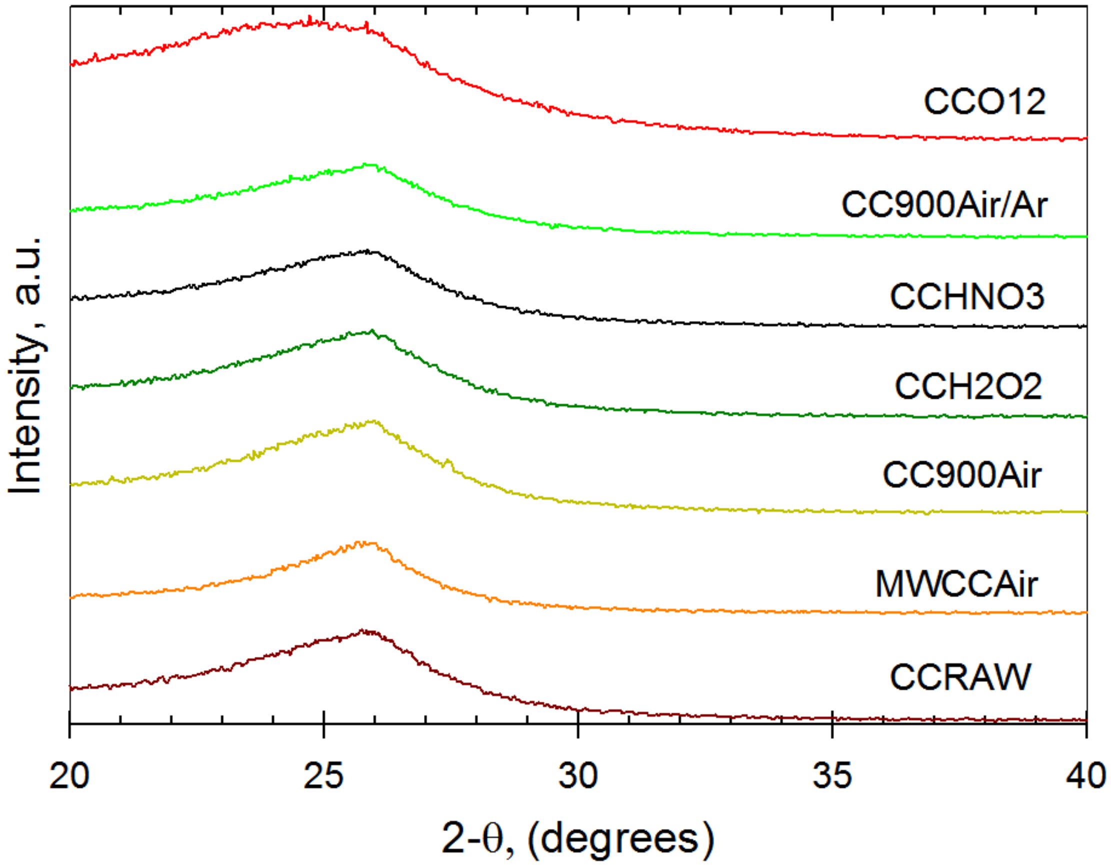

Figure 4.2: The XRD results for the oxidized and the microwaved carbon nanocones as well as for the oxygen-functionalized carbon nanocones from n-TEC (CCO12) and the untreated carbon nanocones (CCRAW).

4.2 Scanning electron microscopy

The surfaces shown from the scanning electron microscope (SEM) images, Figure 4.3 to 4.12, have no distinct differences. There are many discs present, as well as carbon black in some areas. The CCRAW cast in Figure 4.8 shows sign of carbon black bound to the cone surface. The cycled carbon anode of untreated carbon in Figure 4.12 has had a very visible alteration of the surface compared to the untreated cast in Figure 4.8.

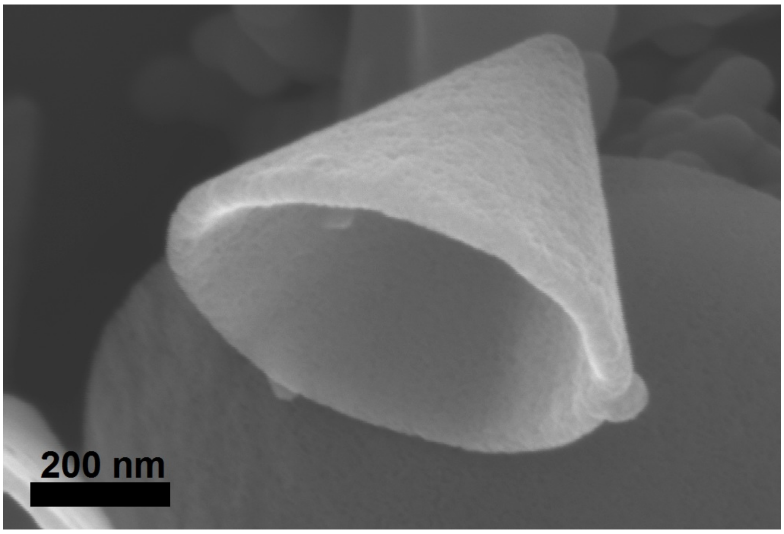

Figure 4.3: SEM images of the heat oxidized carbon nanocones (CC900Air).

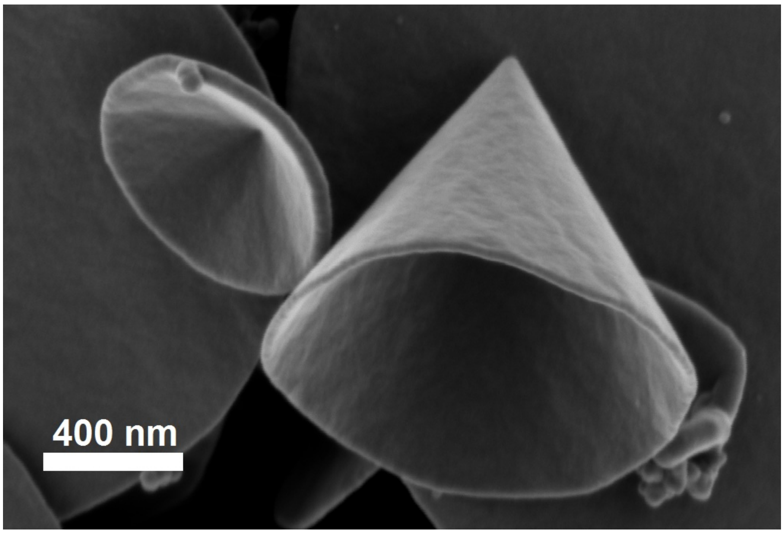

Figure 4.4: SEM images of the carbon nanocone powder oxidized with HNO_3.

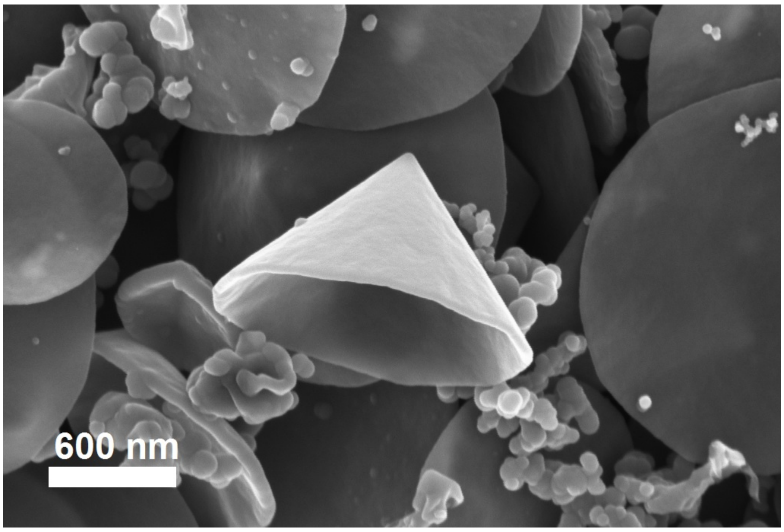

Figure 4.5: SEM images of the carbon nanocones powder oxidized with H_2O_2.

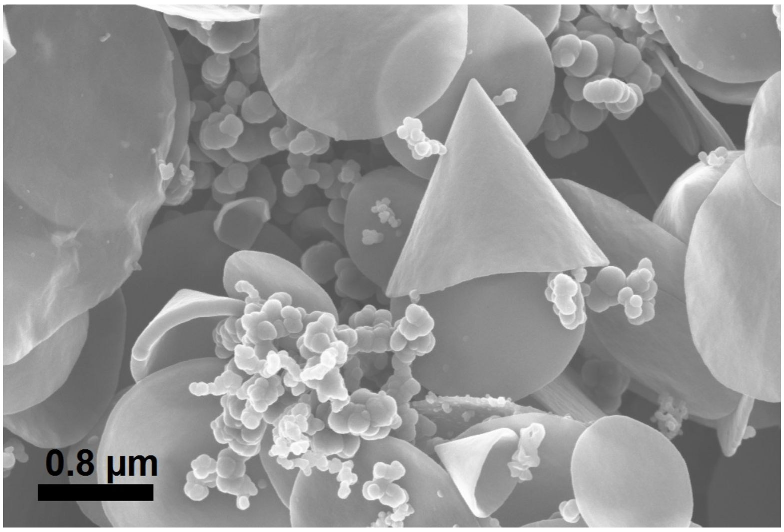

Figure 4.6: SEM of the heat treated powder HTCC950.

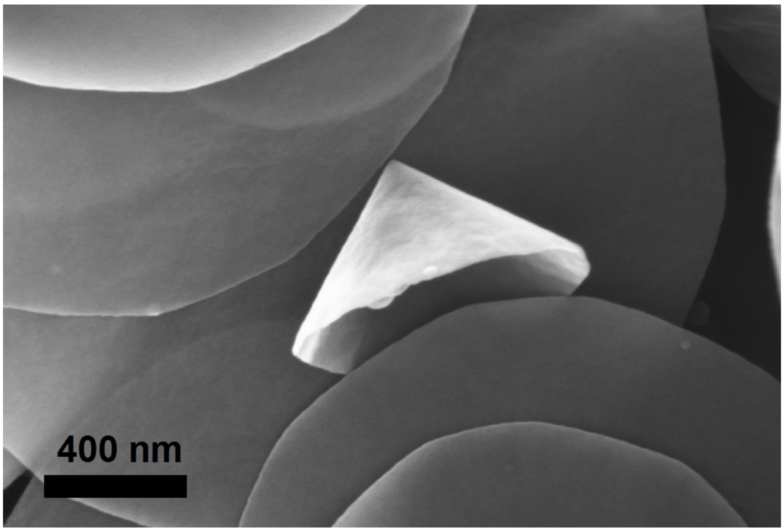

Figure 4.7: SEM of the heat treated powder HTCC1800.

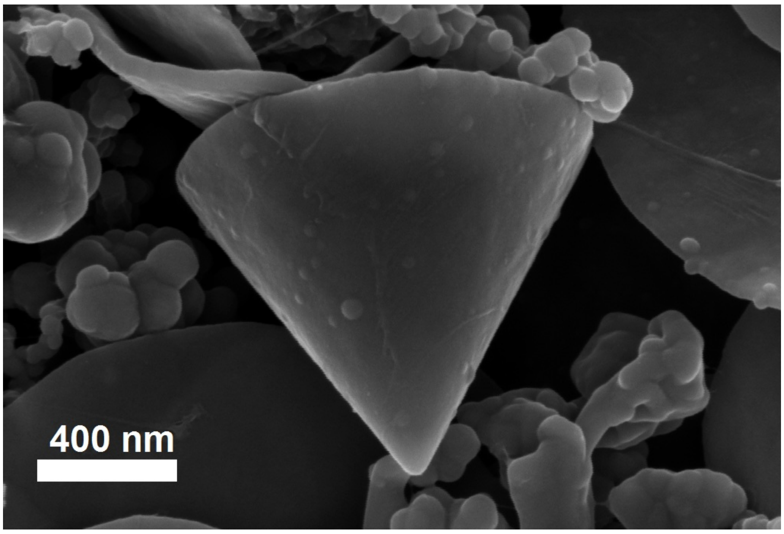

Figure 4.8: SEM images of the CCRAW-20.2 cast.

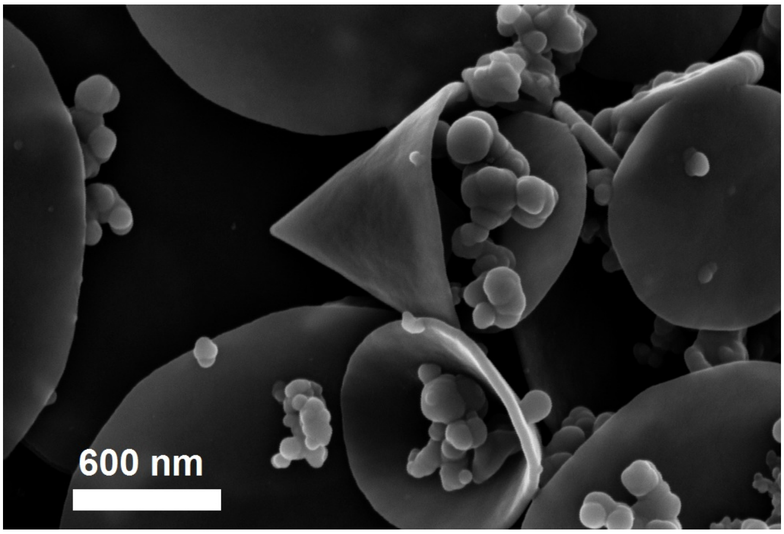

Figure 4.9: SEM images of a CCO12 cast.

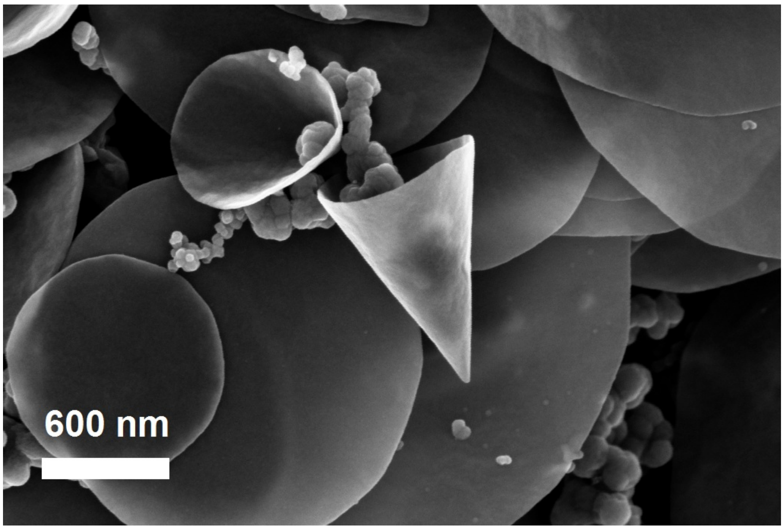

Figure 4.10: SEM images of a HTCC1800 cast.

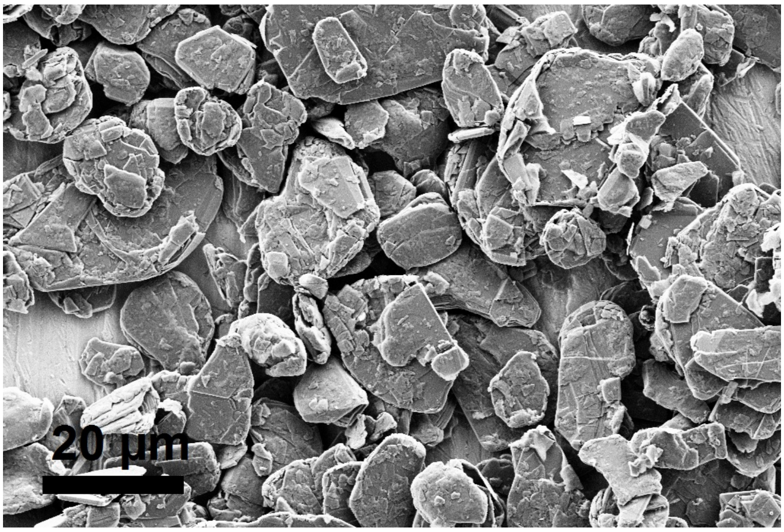

Figure 4.11: SEM of the graphite powder SLP30.

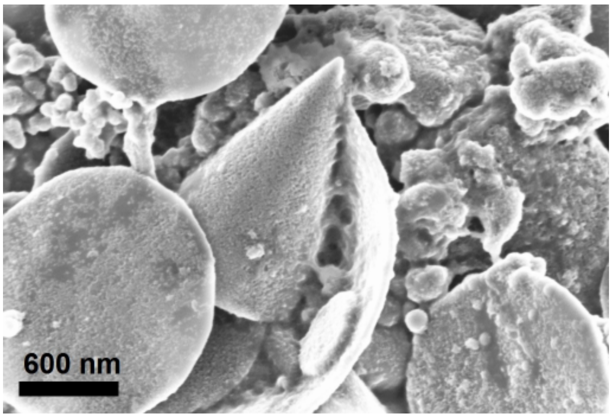

Figure 4.12: SEM image of a cast, CCRAW-20.2, which have been cycled one time.

4.3 Surface area measurements

The surface areas of the different carbon cone powders are found in Table 4.1.

The high temperature (2700°C) heat treated carbon samples which were treated in argon had lower surface area than the untreated carbon powders. The powders that were treated at 900°C in air had considerably higher surface area than the untreated powder. The exception was the CC900Air/2700 which still had its low surface area. It had a slight decrease in surface area compared to HTCC2700. All other powders got just a slight increase in surface area, compared to the untreated powder.

Carbon cone powder	Surface area (m^2/g)
CCRAW	19.87 ± 0.03
HTCC2700	14.83 ± 0.16
HTCC1800	17.66 ± 0.13
HTCC950	20.89 ± 0.01
HTCC900Ar/Air	80.87 ± 0.86
HTCC900Ar/Ox	21.96 ± 0.04
CC900Air	96.69 ± 1.01
CC900Air/2700	13.25 ± 0.11
CCH2O2	20.08 ± 0.02
CCHNO3	21.49 ± 0.03
MWCCAir	20.67 ± 0.02
SLP30	4.78 ± 0.01

Table 4.1: Surface area results of BET measurements of the different carbon powders.

4.4 Fourier transformed infrared spectroscopy (FTIR)

The Fourier transformed infrared spectroscopy results are shown in Figure 4.13 to 4.16. Table 4.2 shows the transmittance minimas, which are the wavenumbers where the characterized materials have absorbed the infrared radiation.

Carbon cone sample	Wavenumber minimas (cm^{-1})
CCRAW	3489, 2950, 2721, 2112, 1945, 1766, 1599, 1579, 1447, 1384, 1200, 899, 748, 692, 651, 604, 557
HTCC2700	3470, 2878, 1777, 1771, 1471, 1397, 1136
HTCC950	3487, 2914, 2120, 1952, 1872, 1776, 1600, 1580, 1453, 1384, 1161, 899, 749
MWCCAir	3490, 2878, 2732, 2122, 1942, 1868, 1774, 1601, 1581, 1469, 1393, 1153, 908, 749
MWCCAr	3496, 2925, 2727, 2120, 1952, 1770, 1600, 1580, 1463, 1398, 1363, 1223, 900, 748, 705, 604, 559
CC900Air	3400, 2961, 2924, 1583, 1388, 1368, 1157
CCH2O2	3476, 2981, 2910, 1789-1798, 1729, 1584, 1481, 1410, 1046, 973, 793
CCHNO3	3542-3472, 2973, 2868, 1716, 1602*, 1579*, 1459, 1385, 902, 746
CCO12	3536-3486, 2962-2872, 2722, 2332, 2112, 1947, 1743, 1578, 1463, 1198, 968, 908, 744
SLP30	3360, 2915, 1583, 1430, 1384, 1165, 1124
CCRAW-20.2-2	3441, 2967, 2927, 2857, 2787, 2362, 2337, 1585, 1435, 1385, 1365, 1246, 1141, 917-880, 788, 618
CC900Air/2700-1	3406, 3004, 2938, 1989, 1809, 1777, 1651, 1584, 1558, 1484, 1409, 1368, 1311, 1196, 1087, 970, 904, 841, 780, 730, 599
CC900Air/2700-2	3406, 3004, 2938, 1989, 1809, 1777, 1651, 1584, 1558, 1484, 1409, 1311, 1196, 1171, 1087, 970, 904, 841, 780, 730, 599

Table 4.2: FTIR results taken from the spectra in Figure 4.13 to 4.16. *These minimas were found by zooming in on the area to find it, so they represent very weak signals.

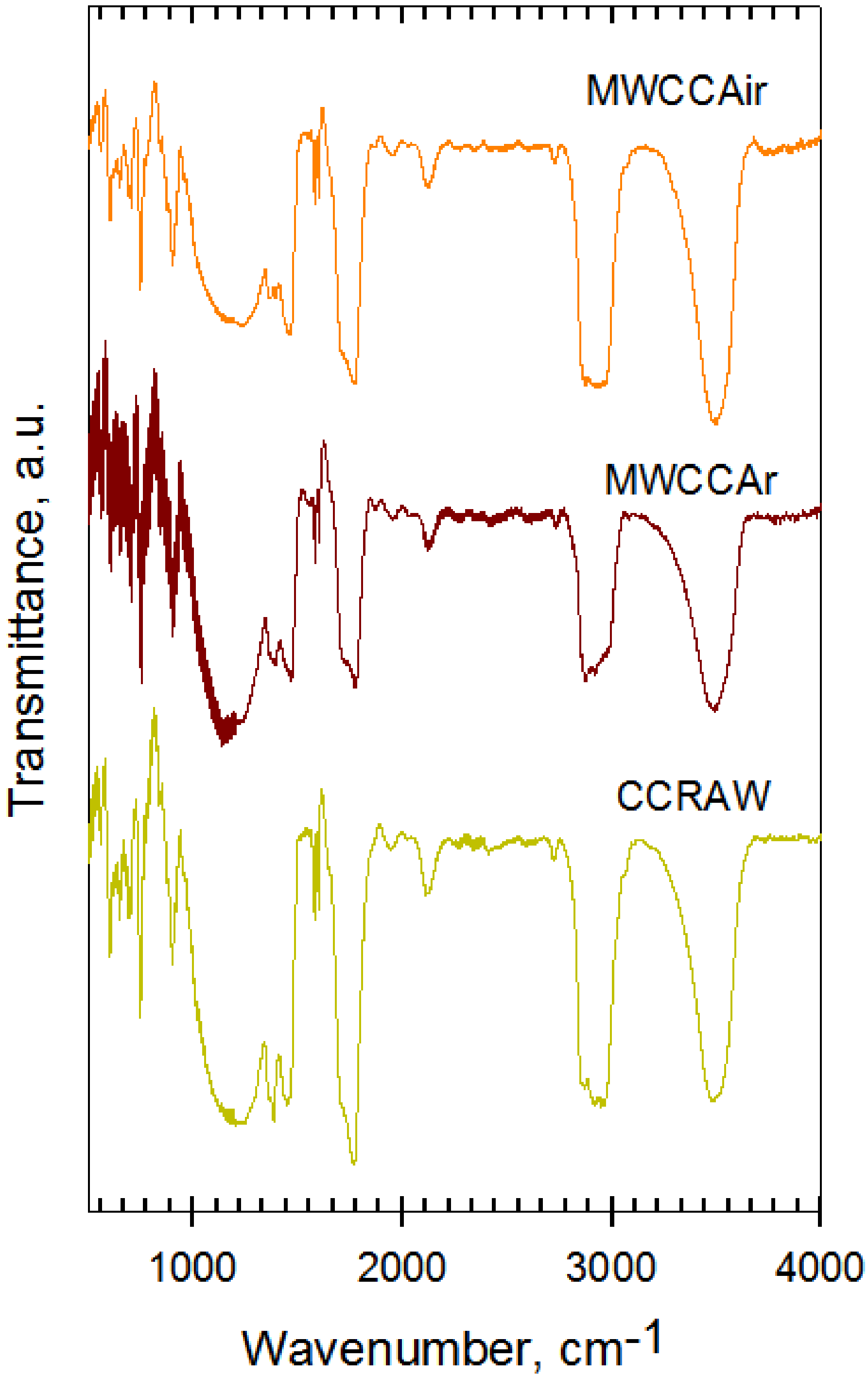

Figure 4.13: FTIR spectra of the microwaved carbon nanocones and the untreated powder (CCRAW).

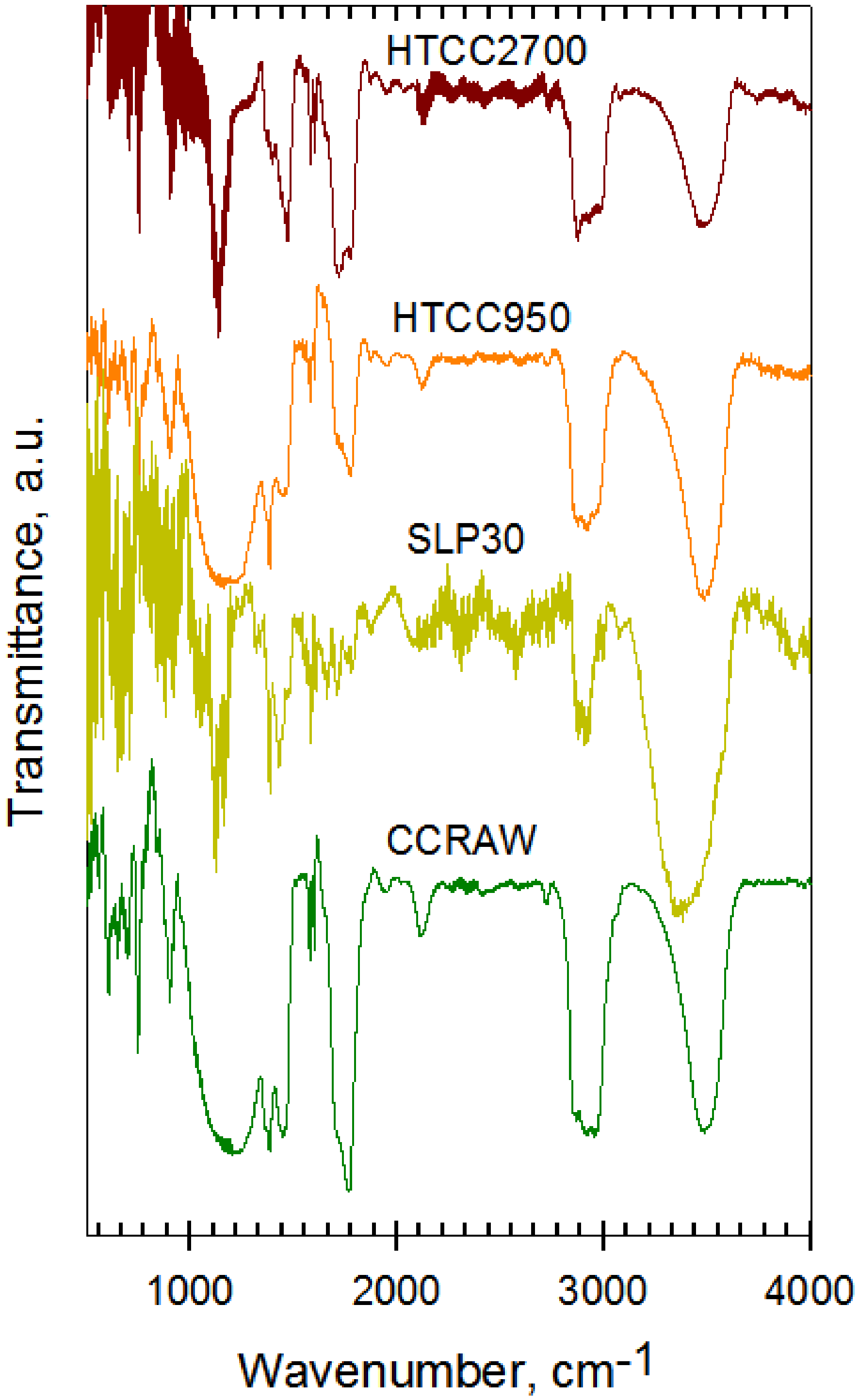

Figure 4.14: FTIR spectra of the heat treated carbon nanocones, the SLP30, and the untreated powder (CCRAW).

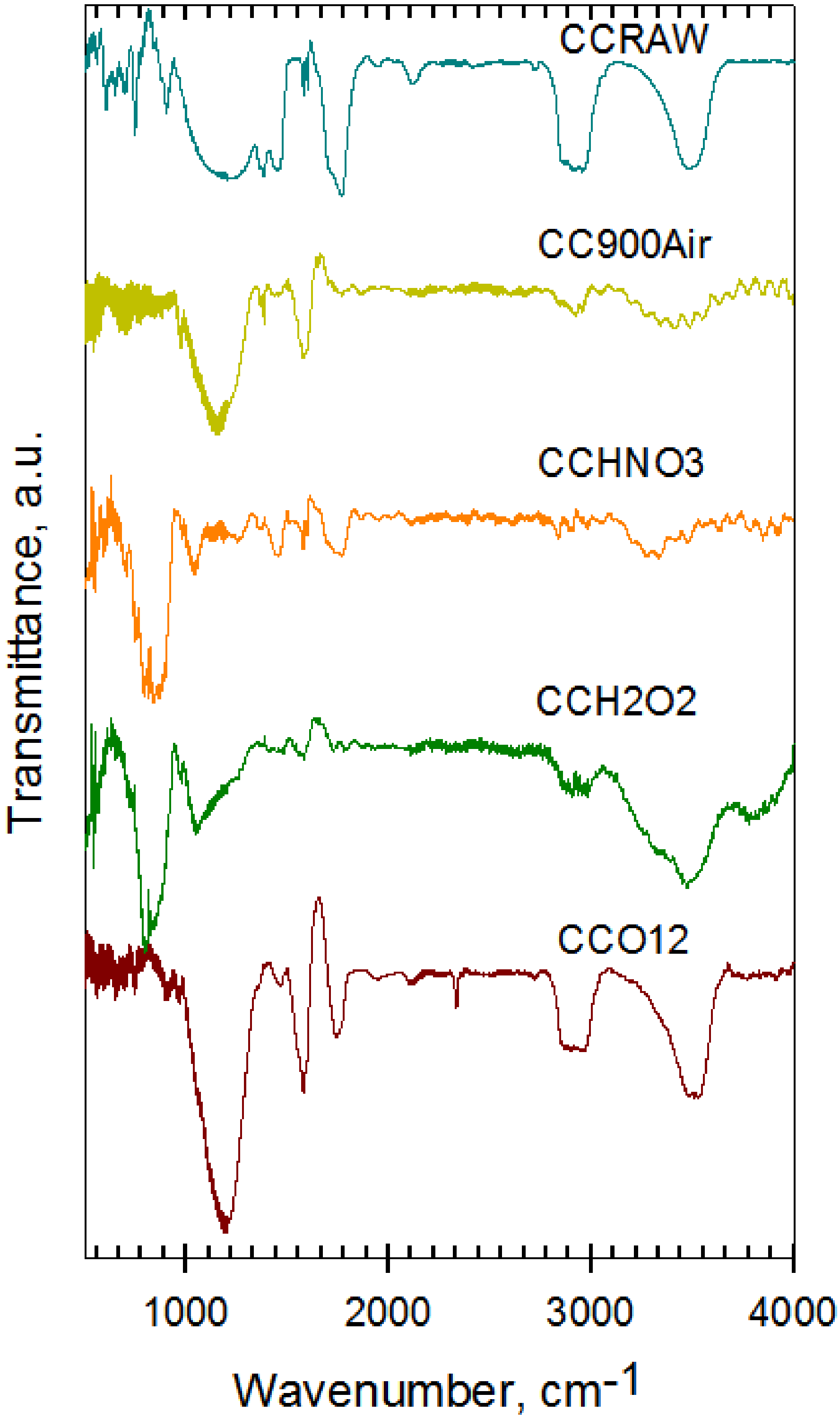

Figure 4.15: FTIR spectra of the untreated powder (CCRAW), the oxidized carbon nanocones, and the oxygen functionalized carbon nanocones from n-TEC (CCO12).

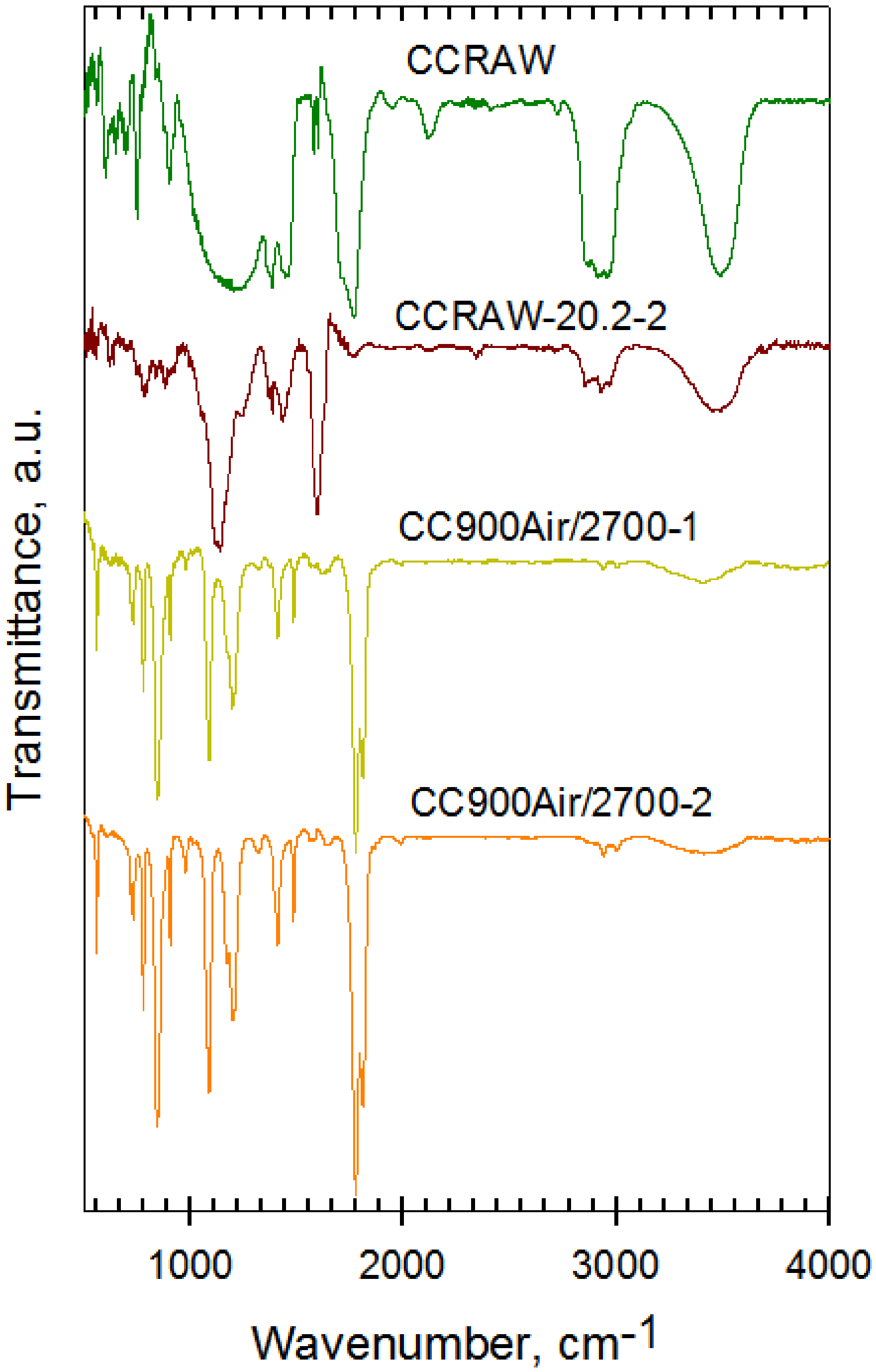

Figure 4.16: FTIR spectra of the untreated powder (CCRAW) and the cycled carbon nanocone electrodes from three batteries.

4.5 Battery characterization

The results of the battery characterization is shown in Table 4.3. The first cycles of a representative battery from each parallel tested are shown in Figure 4.17, Figure 4.18, and Figure 4.19. The full cycles for every battery can be found in section A.1.

Batteries	Thickness (μm)	C$_{init}$ (mAh/g)	C$_{irr}$ (mAh/g)	OCV (V)	e$_{Col}$ (%)	C$_{irr}$ loss (%)
HTCC2700-250μm-2	64	365	94	2.54	74.2	25.8
HTCC2700-250μm-3	67	382	117	1.38	69.4	30.6
HTCC2700-150μm-1	54	370	108	2.44	70.8	29.2
HTCC2700-150μm-3	52	331	78	1.87	76.4	23.6
MWCCAir-25-1	58	616	273	1.87	55.7	44.3
MWCCAir-25-2	58	596	270	2.33	55.6	45.4
HTCC950-150μm-1	74	803	292	1.49	63.6	36.4
HTCC950-150μm-2	91	1063	380	1.22	64.2	35.8
HTCC950-150μm-4	72	599	217	3.24	63.8	36.3
CC900Air-1	58	914	462	3.09	49.5	50.5
CCH2O2-1	67	601	200	1.11	66.8	33.2
CCHNO3-1	71	810	317	2.69	60.9	39.1
CCRAW-20.2-2	43	632	253	1.56	60.0	40.0
CC900Air/2700-1	48	634	135	2.72	68.1	31.9
CC900Air/2700-2	56	634	206	1.87	67.5	32.5
SLP30	42	526	70	2.57	86.8	13.2

Table 4.3: Results from the first charge/discharge cycle. Abbreviations: C$_{init}$ - initial discharge capacity, C$_{irr}$ - irreversible capacity, OCV - open circuit voltage, and e$_{Col}$ - Columbic efficiency.

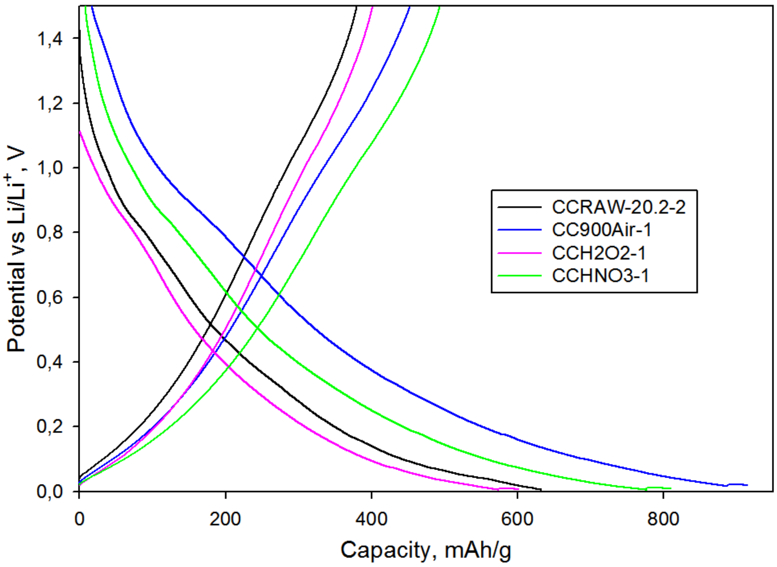

Figure 4.17: The first cycle capacity results of the batteries made of oxidized carbon nanocone powders. The CCRAW result is added for comparison.

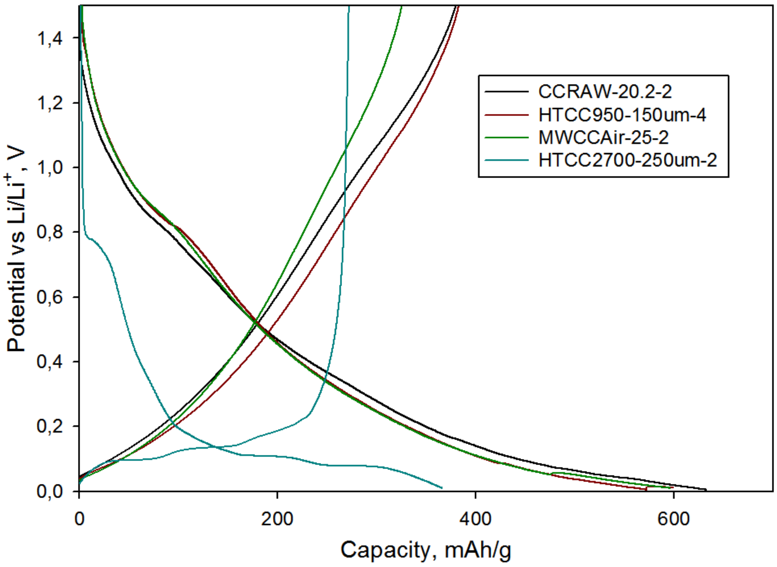

Figure 4.18: The first cycle capacity results of the batteries made of the heat treated carbon nanocones; HTCC2700 and HTCC950, as well as the carbon nanocones treated with microwaves in air, MWCCAir. The CCRAW result is added for comparison.

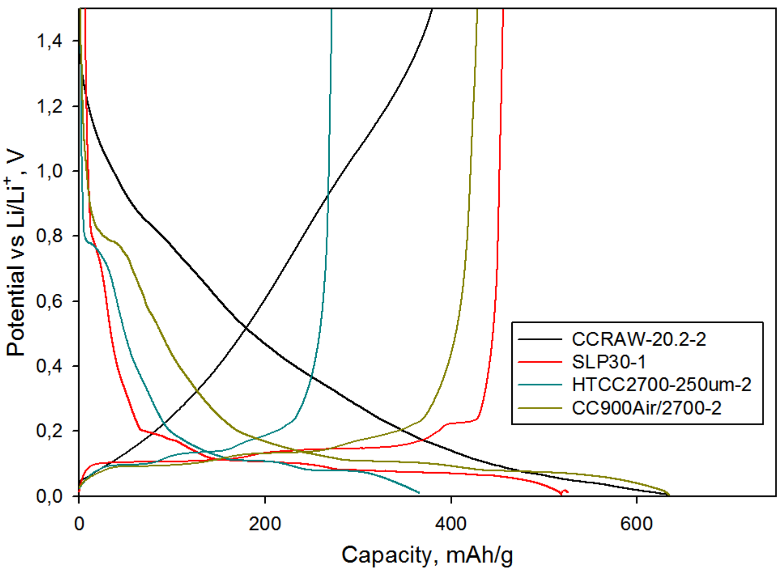

Figure 4.19: The first cycle capacity results of the batteries made of the heat treated carbon nanocones, HTCC2700, the oxidized heat treated carbon nanocones, CC900Air/2700, and graphite, SLP30. The CCRAW result is added for comparison.

Chapter 5

Discussion

5.1 X-ray Diffraction

The degree of crystallinity of the untreated powder is not very high. This is an expected result, as the carbon nanocones is believed to consist of some layers of graphene surrounded by amorphous carbon. The same goes for the discs. The carbon black has a turbostratic structure. Upon heat treatment the crystallinity changes for these types of soft carbon. Heat treatment at 950°C in argon atmosphere for one hour did not change the crystallinity. A change is very visible in the HTCC1800. This powder has clearly more crystalline carbon than the the rest, with exception of HTCC2700, CC900Air/2700 and SLP30. The HTCC2700 shows more signs of being crystalline than the HTCC1800, so a crystallization process is going on between 1800 and 2700°C, and it is faster at 2700°C. The lower the temperature, the slower the crystallization process is going. The SLP30 consists of graphite, which is crystalline carbon. The more crystalline the powder is, the sharper the peaks should be. Thinning is another effect on XRD spectras and correlates to the crystallite size. This clearly explains the XRD results of the SLP30 powder and it can be used as a reference for the crystallinity of the carbon nanocones. The oxidization of the HTCC2700 seems to have done nothing to the crystallinity, which can be observed in the diffractograms for the CC900Air/2700 and HTCC2700.

Another visible trend is peak shift. Peak shifts are present as the carbon powders get more crystalline. This indicates, by using Bragg's law, that the distance between the lattice planes are decreasing. Decreased lattice plane spacing would indicate a denser crystal. Denser crystals should have less surface area per mass than the less dense crystals, and this can be tested out with surface area tests, like a BET measurement. Another possibility for peak shift is sample displacement. The X-ray beam has a reference point in which it calculates its signals from. If the sample should be misaligned this could affect the signals and give peak shifts. Still, this is not very likely as there is no peak shift in the diffractograms for the powders that were not heat treated.

There are also reports of peak shift in the literature. When carbons where annealed at different temperatures by Tai *et al.* , they observed peak shifts as the annealing temperature increased [84], as well as smaller width of the peak with higher heat treatment. Peak shift was said to be due to uniform strain during from the unburned carbon on the crystallization process [84]. The peak width shrinkage was due to non-uniform strain from the same process [84]. Taking this in consideration, the peak shift is most likely due to the annealing, and not sample displacements.

5.2 Scanning electron microscopy

The images retrieved with SEM shows little difference in the surface of the carbon nanocones. CC900Air shows rougher surface than the other ones. This can indicate that during the oxidization in air at 900°C parts of the amorphous layer were burnt away, creating a rougher surface than the untreated carbon. The HTCC1800 is not visibly more crystalline than the untreated carbon, which is an indication that the degree of crystallinity is not as high as the HTCC2700 and SLP30. The SLP30 powder is small, μm-sized grains of graphite. XRD results were indicating crystalline particles that could be larger than the carbon nanocones, and this is clearly the case. None of the other surfaces have the sharp, abrupt edges like SLP30 surface. This indicates that none of the powders have the same, crystalline surface.

The casts are not looking very differently from the powders. The binder, PVDF, is likely to be well dispersed, as the polymers are not conductive and would have been visible as charge would have been built up in possible PVDF clusters. No such clusters were found. PVDF binds very well to carbon [48, 47]. Since both carbon black and carbon nanocones and discs are carbon, the possibility that PVDF binds these together is very likely. Another sign of the binder being well dispersed and doing what it is supposed to do it the mechanical strength of the cast. The casts can withstand some mechanical deformation without flaking off or being destroyed.

Carbon black is present in all powders, except the SLP30. They make small clusters and are in many cases situated on or inside the carbon nanocones. Some carbon black particles looks like they have been adsorbed on the amorphous carbon nanocone and disc surfaces. This is also the case at some of the casts, which is possibly due to the PDVF. The absorbed carbon black in the powders might be explained by the fact that carbon black are particles of very small turbostratic particles. These particles could make clusters with the amorphous surface of the carbon nanocones and discs instead of other carbon black particles.

SEM images of the cycled anode differs the most from the other pictures taken. Here the surface is clearly altered. Most of the amorphous carbon surface is covered with a layer that seems to be porous. This layer is called the solid electrolyte surface (SEI). This layer is made as a result of reactions between the carbon and electrolyte.

The electrolyte has been decomposed into new, organic and inorganic, products which have been deposited on the carbon surface. The results of this can be seen on the carbon nanocones and discs as well as on the surface of the carbon black. The coverage of the SEI does not seem to be complete, which can be a problem for further cycles, as more lithium and electrolyte will be used in the process of creating more SEI. This could also be sites for exfoliation of the carbon material. The usual case is that the SEI uses more than one cycle to get complete coverage. In this case the sample was only cycled one time.

SEI is needed to protect the carbon from exfoliation. The SEI is also unwanted when it becomes thick, as this prevents lithium ions from intercalating into the carbon. The important point is to get a stable, uniform, thin SEI with good, and efficient coverage. However, the SEI formation on the CCRAW anode seems to lack in uniformity. It does not have an even distribution in thickness and coverage. A reason for this could be the amorphous carbon surface. Amorphous carbon consists of randomly orientated carbon. This can give non-uniformal distribution of basal and edge planes. The basal planes is the dominating site for SEI formation, where as the edge planes are the major site for exfoliation [34]. SEM images shows that the basal planes are more exposed to the electrolyte than the edge planes. Non-uniform distribution of SEI on an amorphous surface of carbon could be caused by possible non-uniform distribution of the two planes on the carbon nanocone, discs and carbon black surfaces. More crystalline carbon would have more uniform distribution of the planes, which would make the SEI formation easier to control.

5.3 Surface area measurements

The surface area of the powders were relatively similar (within 12% of the CCRAW), with the exception of HTCC2700, SLP30 and CC900Air. CC900Air might have this high surface area because it has become more porous compared to the untreated powder. The oxidization process it has been through will remove some of the carbon. This was clearly seen on the alumina crucible used to heat treat the carbon. The crucible had some areas with carbon on it prior to the treatment, but is was looking like it was unused after the treatment. The SEM showed that the surface had areas that looked like small holes in the amorphous carbon of the cones and discs. These pores could be the reason for the larger surface area. The surface area is about 5 times higher than for the untreated powders, so there is a substantial difference. Smith *et al.* have reported that oxidized carbon black increases its surface area to six times the untreated value [85]. The carbon black was first thermally graphitized and the oxidized. This is similar with the results for the CC900Air, with the exception of graphitization. Smith *et al.* also mentions SEM images that could indicate an increase in porosity of their carbon black. This supports the observation of the more porous carbon nanocone and disc surfaces. There is no visible decrease in the particle size, so this could not explain the large increase in surface area. The mass of the powder was only 48% of the original mass when the oxidization process was finished, indicataing that porosity is the surface area increasing factor.

HTCC2700 is very crystalline, and the XRD shows that the crystal plane distance is smaller than for the less crystalline powders. This makes it denser, and hence the surface area would decrease. Still, the SLP30 has an even lower surface area. This can be explained by the grain size. SLP30 grains are fairly larger than the carbon nanocones and discs. Compared to the CCRAW, the HTCC2700 is smoother and denser on the surface. There might be some traces of porosity, which partially gives the HTCC2700 higher surface area than SLP30. The HTCC1800 has even higher surface area than HTCC2700. This is possibly due to the fact the degree of graphitization is lower.

The HTCC2700 was also oxidized at 900°C, but in this case the surface area did not increase. It decreased. This case is also similar with results from Smith *et al.* [85]. They reported that the carbon black which were heat treated in an inert atmosphere at 2700°C and then oxidized did not increase its surface area. The reason is thought to be the reduction of active sites where oxidization can occur. Instead the decrease can be due to oxidization of species that are adsorbed on the surface, making the surface rougher.

5.4 Fourier transformed infrared spectroscopy (FTIR)

5.4.1 Carbon powders

The Fourier transformed infrared spectroscopy results performed on the different samples showed no major differences. The oxidized samples CCHNO3 and CCH2O2 had some different patterns compared to the rest of the powders. The SLP30 also had a different pattern compared to the carbon nanocone powders, but it too had a couple of distinct similarities. The local minimas are simply referred to as signal peaks or signal peak bands.

Starting in the high wavenumbers, the FTIR spectras showed that all the samples had absorption bands in the vicinity of 3400 cm^{-1}. This is mainly due to O−H-groups and absorbed water [57]. KBr, which was used as the pellet material, is hygroscopic. The water signal peaks could very likely come from the KBr as well as from the carbon powders. Presence of moist air could also affect the results and cause these O−H-groups to be visible. After some time, more precautions were taken. The KBr was stored in a glove box with argon atmosphere instead of in an exicator, and the pellet pressing was done with a zip-lock bag with argon gas to ensure minimal exposure to air. Still, the same water signal peak band was present. This presence could indicate that there is absorbed water on the carbon powders to start with, and this was hard to remove without going through a thorough drying process.

The next interesting band were situated between 2950 and 2850 cm^{-1}. Aliphatic C$-$H-bonds gives signal peaks at 2950, 2925 and 2860 $cm-1$ [64]. As the powders are produced from residues from oil and gas, the possibility of having aliphatic carbon present is high, especially in the amorphous parts of the carbon. It is therefore very likely that all these signal peaks in the samples are coming from C$-$H-bonds at the surface of the particles.

All the powders, with an exception of HTCC2700, have signal peaks present between 1860 and 1650 cm^{-1}. These have been said to be related to carbonyl and carboxyl groups. C=O-bonds can be a main contributor to these signal peaks [60]. C=O-bonds in aromatic molecules gives signal peak bands from 1700 to 1680 cm^{-1} [60], but none of the powders have signal peaks in this region. The signal peaks of the powders were all gathered around 1770 cm^{-1}, with an exception of CCHNO3 and CCH2O2. These two powders had signal peaks at 1716 and 1726 cm^{-1}, respectively. Non-aromatic C=O-bonds give signal peaks at 1712 cm_{-1} [60], so it is very likely that the wet chemical oxidization processes have made oxygen bonds on the surface of the carbon nanocone powders. What the high 1700 cm_{-1} wavenumber signal peaks for the other powders represent is difficult interpret. It is most likely a C=O-bond, but from what kind of compound class it derives from is not obvious. γ-lactones have its carbonyl signal peak bands from 1780 to 1760 cm^{-1} [57] and this fits with the signal peaks in the 1770 cm^{-1} region. This indicates that there might be ester groups causing this signal peak. Ketone groups is another possibility, as their signal peaks can shift and usually lies around 1740 cm^{-1} [60].

At around 1580 cm^{-1}, all but HTCC2700 shows a signal peak band. Aromatic ring stretching coupled to conjugated carbonyl groups gives a signal peak at 1580 cm^{-1} [60]. This supports the observations of the earlier mentioned carbonyl groups, and can be seen as very likely. Graphite contains layers of hexagonally organized carbon molecules which looks like a honeycomb pattern. At the plane edge the layers of these hexagons will look like aromatic carbon. This would give signal peak bands similar to what aromatic compounds would which is also observed in this sample. The reason that the HTCC2700 does not show this signal peak can be due to the phenomenon that happens during the heat treatment. Upon heat treatment the edge layers wrap around each other and eventually hides the open edge layers. Hiding the edge layers will remove the aromatic bonds from the surface and the signals will not appear.

Another signal peak that most of the powders (not CC900Air and SLP30) show is situated right above 1460 cm^{-1}. This correspond to the O$-$H-bond in carboxyl groups [60], and is supporting the earlier mentioned carbonxyl group signal peaks.

Signal peak bands from 1390 to 1380 cm^{-1} is found in all powders except CCH2O2 and CCO12. These are likely to be from double bonds in aromatic carbons which gives signal peak bands from 1400 to 1380 cm^{-1} [60]. Friedel *et al.* found out that carbon, which he grinded to powder, had two distinct bands at 1587 and 1362 cm^{-1} [59] which is also found for almost every carbon powder. Friedel *et al.* also found out that there were signal peak shifts of up to around 20 cm^{-1}. This supports the other sources that suggests that this is carbon signal peaks.

There are also several signal peaks below 950 cm^{-1}, and they are most likely to mainly arrive from C−H deformation vibrations in out of plane directions of the aromatic carbon [60]. Noise in some of the lower wave number regions makes interpretation of these regions difficult. These results in this region can therefore not be completely reliable, and some of the signals did not fit very well with any results from the literature. The CCH2O2 and CC900Air had a substantial amount of noise from 4000 to around 2300 cm^{-1}. There is still possible to see the absorption bands around 3400 cm^{-1}. The SLP30 is also affected by much noise, still there were some detectable peaks which are good for use in the characterization.

To summarize the results of the powders, the FTIR showed signs of aromatic carbon, which indicates that there is graphite present. This carbon seems to have a surface with carboxyl- and ketone groups, both the untreated and the treated powders. As this technique cannot give quantitative results, the amount of surface oxygen present on the different powders is impossible to determine. The spectras was looking almost the same, with the exception of CCHNO3 and CCH2O2. Their spectras had a larger signal peak lower that the other powders. This can be caused by groups that were formed during the wet chemical oxidization. These groups were not identified.

5.4.2 Cycled carbon casts

Carbon material from cycled half-cells were also characterized. The materials characterized were CCRAW and CC900Air/2700 electrodes with a solid electrolyte interface (SEI). The goal was to find components corresponding to SEI components in the literature, which is presented in Table 2.1.

Just like the powder samples, the electrodes had bands laying in the vicinity of 3400 cm^{-1}. Apart from being just absorbed water, in the literature there have been reported that peaks between 3000 and 3700 cm^{-1} could be hydroxy groups [72]. Hydroxy groups can derive from reduction products of $(CH_2OCO_2Li)_2$ due to HF which is often present as contamination in $LiPF_6$ [72]. Electrolytes containing ethylene carbonate (EC) usually contains $(CH_2OCO_2Li)_2$ [29], so this supports the possibility of the first signal peak band deriving from other groups than absorbed water.

The CC900Air/2700 had a peak at 2938 cm^{-1}. C−H bonds have a signal peak band in this area around 2900 to 2700cm^{-1} [74]. These bonds can be associated with $ROCO_2Li$ [72, 70] or ROLi [73, 74]. The CCRAW had signal peaks at 2967, 2927, 2857, and 2787 cm^{-1}. The first signal peak, 2967 cm^{-1}, could be a slightly shifted signal peak from ROLi at 2963 cm^{-1} [73]. The two middle ones, 2927 and 2857 cm^{-1}, fits good with $ROCO_2Li$ which have reported signal peak bands of around 2950 and 2850 [72, 70].

The CCRAW electrode also had a signal peak at 2787 cm^{-1}. Alkoxy species in CH_3OLi has a signal peak band from 2820 to 2700 cm^{-1} [72]. This could be a reason for the CCRAW's signal peak, but more generally ROLi has signal peak bands from 2900 to 2700 [74]. The presence of ROLi is made more likely.

Some of the absorption signal peaks between 2000 and 1700 cm^{-1} are similar to the carbon, and not mentioned in the FTIR literature for SEI characterization, so they are most likely signal peaks from the carbon and not the SEI.

At 1651 cm^{-1} the CC900Air/2700 electrode has a signal peak. This matches up with the C=O-group's assymetric stretching vibration peaks from $(CH_2OCO_2Li)_2$ at 1650 cm^{-1} [70] and 1654 [71]. It also supports previous signal peaks. Signal peaks around 1585 for the CC900Air/2600 is the same signal peak as the powder samples showed, so this is most likely corresponding to the carbon and not the SEI. The CC900Air/2700 has a signal peak at 1484 cm^{-1}, this could correspond to a similar signal peak in the carbon powders, but shifted. This signal peak could also be from the C−O bond in the Li_2CO_2 [73, 70, 75].

The CCRAW electrode had a signal peak at 1435 cm^{-1}, which again is more likely to be from the carbon and not the SEI.

At 1409 cm^{-1} the CC900Air/2700 got a signal peak that could correspond to C−O bonds at 1400 cm^{-1} in Li_2CO_2 [77] or CH_2 bonds 1450 to 1400 in $(CH_2OCO_2Li)_2$ [70, 71] and $ROCO_2Li$ [70, 72]. The presence of all three could be plausible, though earlier discussed signal peaks supports $(CH_2OCO_2Li)_2$ and $ROCO_2Li$ more than Li_2CO_2.

Another signal peak that have more than one possibility is the 1385 cm^{-1} signal peak from the CCRAW electrode. This could be a CH_2 bending vibration from $(CH_2OCO_2Li)_2$ [69] or COO^- bending vibration from HCOOLi [69, 79]. The latter is more plausible if there is a signal peak at 790 cm^{-1} as well. Signal peaks in the same vicinity, 1365 cm^{-1} for the CCRAW and 1368 cm^{-1} for the CC900Air/2700, are very similar to carbon signal peaks [59] and are most likely not connected with SEI signal peaks. The 1311 cm^{-1} signal peak of CC900Air/2700 corresponds well with signal peaks between 1320 and 1290 cm^{-1} from C=O-bonds symmetric stretching vibration in $(CH_2OCO_2Li)_2$ [70]. Yet another supporting result for the presence of $(CH_2OCO_2Li)_2$.

There are some indecisive peaks of 1246 cm^{-1} (CCRAW), 1141 cm^{-1} (CCRAW), and 1171 cm^{-1} (CC900Air/2700). These could be results from the carbon material as they are not mentioned in the literature. The 1196 cm^{-1} signal peak from the CC900Air/2700 electrode is most likely to come from the C−F bonds signal peak at 1200 cm^{-1} [73]. Bonds between the binder, PVDF, and the carbon is known to be present [48, 47] and therefore supports this result. At 1087 cm^{-1} the CC900Air/2700 has a signal peak which is likely to derive from C−O-bonds. Which SEI component this corresponds to is not as clear, but alternatives are ROLi [74], $ROCO_2Li$ [74, 70, 73], and $(CH_2OCO_2Li)_2$ [70, 71].

From 970 cm^{-1} and below the carbon could contribute with out of the plane vibrations of C−H-bonds. The signal curve have less noise in this area than the powders had. This makes interpretation more accurate. The CCRAW electrode have a signal peak band from 917 to 880 cm^{-1}. This could correspond to the presence Li_2CO_3 and its bending vibration of CO_3^{2-} at 890 to 870 cm^{-1} [73]. At 841 cm^{-1} the CC900Air/2700 has another signal peak, and this might arrive from OCO_2 bending vibrations, indicating presence of $(CH_2OCO_2Li)_2$ [70] or $ROCO_2Li$.

The 1385 cm^{-1} signal peak had to have a corresponding signal peak at 790 cm^{-1}. CCRAW has a signal peak at 788 cm^{-1}, and the CC900Air/2700 at 780. The latter did not have any signal peaks at 1385 cm^{-1}, so there is more probability that the CCRAW has HCOOLi as a SEI component. Still, it does not exclude the possibility that this is a component in the SEI of the CC900Air/2700 electrode either. Further on, the CCRAW has a signal peak at 618 cm^{-1} and CC900Air/2700 a signal peak at 599 cm^{-1}. These have been present in the powders as well, but still it corresponds well with the presence of Li−O-bonds from LiO_2 [73, 74].

The more signal peaks the different components have that corresponds to the literature, the more likely is the component to be present in the SEI. To summarize the result, there are indications of a couple of SEI components in the used electrodes. The CC900Air/2700 electrodes have many indications on the presence of $(CH_2OCO_2Li)_2$, $ROCO_2Li$, ROLi, Li_2CO_3, and Li_2O. The two first ones have more matching signal peaks than the three latter ones, but there is no possibility of excluding any of them. For the CCRAW electrode, the case is a little different. Possible components here are $(CH_2OCO_2Li)_2$, ROLi, HCOOLi, Li_2CO_3, and Li_2O.

Li_2CO_3 is reported to be a reduction product during cycling above 0.8 V [34] when using EC as a lithium salt solvent. This project used $LiPF_6$ in a 1:1 mixture of EC and diethyl carbonate (DEC). In electrolytes with EC it has been found that the major decomposition product of EC is $(CH_2OCO_2Li)_2$ [29]. There is also said that $(CH_2OCO_2Li)_2$ and Li_2CO_3 are less soluble than ROLi and $ROCO_2Li$ [29]. This could be a reason for the good prescience of signal peaks from $(CH_2OCO_2Li)_2$, but still the $ROCO_2Li$ also has many possible signal peaks present. The FTIR with KBr pellets in not able to determine quantitative measurements, so to what extent the SEI components are present is not known. Only their prescience can be determined.

5.5 Battery characterization

The carbon nanocone batteries of various powders were cycled. First an initial discharge, before a charge was performed. Initial capacities were measured and it varied from 331 to 1063 mAh/g. The highest initial capacity was achieved with the heat treated powder HTCC950, and the lowest was achieved with the heat treated powder HTCC2700. HTCC2700 together with CC900Air/2700 were showing similarities with graphite (SLP30), which is not that strange as XRD results showed that these powders were much more crystalline compared to the other powder. The exception would be the partially graphitized powder HTCC1800, but this was not characterized as an electrode. The HTCC2700 showed results around the theoretical capacity which is 372 mAh/g for LiC_6 [2]. In other words, the HTCC2700 capacity was no better than the theoretical graphite capacity. The Columbic efficiency has been increased from around 55-60 % for CCRAW [8] to around 70-75 % for the HTCC2700. Still not reaching the Columbic efficiency of the commercial graphite, SLP30, at 86.8 %.

The microwave treated powder, MWCCAir, reached a initial capacity about 600 mAh/g. The Columbic efficiency was not any higher than the untreated powder, so the microwave treatment seems to have no positive effect on the carbon nanocones battery performance. In fact is seems that nothing has happened to the microwaved powder, which also is visible in the FTIR spectra. The spectra for the MWCCAir is almost identical to the CCRAW.

Another heat treated powder, HTCC950, had a spread in the initial capacity from 599 to 1063 mAh/g. The thickness is also varying. These two parameters seems to follow each other. The thicker, 91 μm, electrode had the highest capacity, and the thinnest, 72 μm, the lowest capacity. This thickness dependency was also found in HTCC2700, but was far less distinct. The Columbic efficiency is close to 65 %, which is higher than the untreated carbon nanocone results [8]. The heat treatment seems to have reduced the irriversible capacity of the HTCC950 to some extinct, but not close to the SLP30. This indicates that the heat treatment has had an effect on the powder, even though the degree of graphitization was undetectable in the XRD. The FTIR does not show any clear differences in the surface groups of the HTCC950 compared to the CCRAW. This can be explained by the fact that the treatment was done in an argon atmosphere. There were no gases present in the oven that could react, and only the heat would have an impact on the powder. The heat would only graphitize the powder very slowly, but the degree of graphitizing was not high enough to be detectable in the XRD.

The oxidized carbon nanocones were differing in results as well. The CC900Air had an initial capacity of 914 mAh/g, but a Columbic efficiency of only 49.5 %. The wet chemically treated CCHNO3 had an initial capacity of 810 mAh/g and a Columbic capacity of 60.9 %. The latter result was better than the CC900Air, but still just the same result as the CCRAW when looking at the Columbic efficiency. Higher initial capacity was the only improvement for these two latter powders. The last oxidized powder, CCH2O2, had a inital capacity of 601 mAh/g and a Columbic efficiency of 66.8 %. This is an improvement of Columbic efficiency, meaning that the irriversible capacity is reduced compared to the CCRAW. The initial capacity is about the same, so the H_2O_2 have reacted with the surface in a way that has been positive for the creation of the SEI. The irriversible capacity has probably decreased as the SEI components made have been more stable and more efficiently created, thus using less lithium.

The cycling curves of the mentioned powders, with an exception of HTCC2700 and

SLP30, showed the same trend as the CCRAW. Their curves did not have any potential plateaus like the SLP30. Some of the curves showed a small plateau where the SEI is created, between 0.8 to 0.9 V [34]. The oxidized ones had a less visible plateau than the others. The SLP30 and the HTCC2700 on the other hand had very clear plateaus, but there is no visible plateau around the creation potential of the SEI. This might be an indication of the reason for its high Columbic efficiency.

CC900Air/2700 was a powder which showed a plateau in the cycling curves, just like the SLP30 did. This powder was made by oxidizing the HTCC2700 for an hour at 900°C in air. By doing this the idea was to get the combination of the high capacity of the CC900Air and the high Columbic efficiency of the HTCC2700. The result was a initial capacity 634 mAh/g for both electrodes, and an Columbic efficiency of around 68 %. This is an increase in the Columbic efficiency, compared to the CCRAW, but not as good as the HTCC2700. Compared to the CC900Air, the initial capacity has been lowered, and compared to CCRAW it is unchanged. If compared to graphite, SLP30, the capacity has been increased, but the Columbic efficiency is not as high. The heat oxidizing process seems to improve the capacity for the graphitized carbon nanocones. The FTIR spectra of both the CC900Air and HTCC2700 is not very different from the CCRAW, so this could indicate that there is no great difference for the CC900Air/2700 either, but since this powder was not characterized this is mere speculations. The XRD results show that the CC900Air/2700 have kept its crystallinity.

The BET measurements showed that SLP30 had the lowest surface area, and then CC900Air/2700 and HTCC2700 followed. These two latter were the best electrodes, especially in the combination of having similar curves at the SLP30 and having improved Columbic efficiency. The curves of the other powders are not as desirable, as they have no stable potential plateau. This makes it reasonable to exclude the continuation of testing them, as the curves reveals that they are undesirable. The FTIR spectra of the CC900Air/2700 showed stable SEI components, which again is desirable so that the electrode is protected against exfoliation and further SEI formation. High surface area is not desirable as the more surface area, the more SEI needs to be made to protect the electrode. SEI uses electrolyte components and lithium, and the irreversible capacity increases. This can explain why the CC900Air has the low Columbic efficiency, and partially the higher Columbic efficiency of the CC900Air/2700 and HTCC2700.

Graphite is not the only comparable anode material. There are numeral reports of different carbon, silicon and composite anode materials. Carbon spheres in the size range of 6.5 μm showed an initial capacity of 430 mAh/g [32]. Another carbon anode material was optimized by controlling pore and particle size and achieved 95 % Columbic efficiency and a specific capacity of 360 mAh/g [19]. Adding different amounts of silicon to graphite has shown to give higher capacities to the material [56]. These results varied from 520 mAh/g with 91 % Columbic efficiency for 5 $wt\%$ silicon to 1675 mAh/g with 74 % Columbic efficiency for 40 $wt\%$ silicon. These results show that there are possibilities for increasing the Columbic capacity for the carbon nanocones, and that the initial capacity results are fairly good compared to graphitized carbon anodes.

Chapter 6

Conclusion

This work has shown that the carbon nanocones from n-TEC are working as carbon anodes in lithium ion batteries. Treatment of the powders was done to see which effect this could have on the performance of the anodes. Oxidization of the carbon nanocones was done, but with mixed results. The oxidization with H_2O_2 and HNO_3 did not enhance the performance, though it did alter the surface groups. The last oxidized parallel, CC900Air, did have an increase in the initial capacity, but the Columbic efficiency went down.

The microwaved carbon nanocones, MWCCAir, and the heat treated HTCC950, did not improve much either. The latter had an increase in capacity compared to the untreated carbon nanocones. The Columbic efficiency for the MWCCAir went down and for the HTCC950 it had a slight increase, which means that the heat treatment worked better than the microwave treatment on improving the battery performance.

The high temperature heat treated carbon nanocones, HTCC2700, was working similar to the graphite. Its capacity was situated around the theoretical capacity for LiC_6 at 372 mAh/g. The Columbic efficiency was also increased compared to CCRAW. By oxidizing this powder in air (CC900Air/2700) the capacity increased up to 634 mAh/g, and the Columbic efficiency decreased from 70-75 % to 68 %. This was a substantial improvement. The other improvement from the CCRAW was the cycling curves. They went from looking like a circular arc, as they did for all other powders except the HTCC92700 and CC900Air/2700, to having a plateau after a steep descent. This latter curve shape is desirable, as this means the electrode can hold a stable potential over time.

Other characteristics of the best performing anodes was the high crystallinity found with the X-ray diffraction and the lower surface area found with BET measurements. These are important characteristics which in this case improved the performance and should be further investigated.

The solid electrolyte interface (SEI) on the carbon electrodes were also investigated. The result was finding traces of common components like $(CH_2OCO_2Li)_2$ and Li_2CO_3.

These were reported to be common to find on cycled electrodes which used some of the electrolyte components that were used in this project. The $(CH_2OCO_2Li)_2$ are also a very stable SEI component, meaning that the SEI for the carbon nanocones batteries are solid and protective.

6.1 Further work

Further work for the carbon nanocone anodes should be to further investigate different treatment methods for the HTCC2700. The treatments should be characterized further with emphasis on identify the differences more thoroughly. AC impedance spectroscopy characterization should be done on the HTCC2700 and CC900Air/2700 casts.

The continuation of SEI characterization should also be pursued further to better understand the processes that are going on the surface and get an understanding on what can be done with the surface to increase the efficiency of the SEI formation during the initial cycle.

Bibliography

[1] J.-M. Tarascon and M. Armand, "Issues and challenges facing rechargeable lithium batteries," *Nature*, vol. 414, pp. 359–367, 2001.

[2] A. K. Shukla and T. P. Kumar, "Materials for next-generation lithium batteries," *Current Science*, vol. 94, no. 3, pp. 314–331, 2008.

[3] R. A. Leising, M. J. Palazzo, E. S. Takeuchi, and K. J. Takeuchi, "Abuse testing of lithium-ion batteries: Characterization of the overcharge reaction of licoo[sub 2]/graphite cells," *Journal of The Electrochemical Society*, vol. 148, no. 8, pp. A838–A844, 2001.

[4] V. A. Sethuraman, L. J. Hardwick, V. Srinivasan, and R. Kostecki, "Surface structural disordering in graphite upon lithium intercalation/deintercalation," *Journal of Power Sources*, vol. 195, pp. 3655–3660, 2009.

[5] M. Ge and K. Sattler, "Observation of fullerene cones," *Chemical Physics Letters*, vol. 220, no. 3-5, pp. 192 – 196, 1994.

[6] A. Krishnan, E. Dujardin, M. M. J. Treacy, J. Hugdahl, S. Lynum, and T. W. Ebbesen, "Graphitic cones and the nucleation of curved carbon surfaces," *Nature*, vol. 388, pp. 451–454, 1997.

[7] J. Hugdahl, K. Hox, S. Lynum, R. Hildrum, and M. Norvik, "Patent; fremgangsmåte for produksjon av mikrodomene grafittiske materialer," 2008.

[8] M. U. Nagell, "Carbon nanocones as anode material in lithium ion batteries," December 2010. Project course report.

[9] M. G. Kim and J. Cho, "Reversible and high-capacity nanostructured electrode materials for li-ion batteries," *Adv. Funct. Mater.*, vol. 19, pp. 1497–1514, 2009.

[10] A. Patil, V. Patil, D. W. Shin, J.-W. Choi, D.-S. Paik, and S.-J.Yoon, "Issue and challenges facing rechargeable thin film lithium batteries," *Materials Research Bulletin*, vol. 43, no. 8-9, pp. 1913–1944, 2008.

[11] "Battery physics - ev physics." http://www.cameronsoftware.com/ev/EV_Battery Physics.html. Cameron Motor Works Electric Vehicle Conversion, August 2004, Information retrieved 09.11.2010.

[12] K. Zaghib, A. G. J. Shim and, P. Charest, and K. A. Striebel, "Effect of carbon source as additives in lifepo4 as positive electrode for lithium-ion batteries," *Electrochem. Solid-State Lett.*, vol. 8, no. 4, pp. A207–A210, 2005.

[13] S. H. Ng, C. Vix-Guterl, P. Bernando, N. Tran, J. Ufheil, H. Buqa, J. Dentzer, R. Gadiou, M. E. Spahr, D. Goers, and P. Novák, "Correlations between surface properties of graphite and the first cycle specific charge loss in lithium-ion batteries," *Carbon*, vol. 47, pp. 705–712, 2009.

[14] C.-G. Wu, M.-I. Lu, C.-C. Tsai, and H.-J. Chuang, "Pvdf-hfp/metal oxide nanocomposites: The matrices for high-conducting, low-leakage porous polymer electrolytes," *J. Power Sources*, vol. 159, pp. 295–300, 2006.

[15] T. Xu, W. Wang, M. L. Gordin, D. Wang, and D. Choi, "Lithium-ion batteries for stationary energy storage," *JOM*, vol. 62, no. 9, pp. 24–30, 2010.

[16] D. Choia, D. Wanga, V. V. Viswanathana, I.-T. Baeb, W. Wanga, Z. Niea, J.-G. Zhanga, G. L. Graffa, J. Liua, Z. Yanga, and T. Duongc, "Li-ion batteries from lifepo$_4$ cathode and anatase/graphene composite anode for stationary energy storage," *Electrochem. Commun.*, vol. 12, no. 3, pp. 378–381, 2010.

[17] L. Sun, C. C. Chan, R. Liang, and Q. Wang, "State-of-art of energy system for new energy vehicles," in *IEEE Vehicle Power and Propulsion Conference (VPPC)*, 2008. September 3-5, 2008, Harbin, China.

[18] G. T. K. Fey, D. C. Lee, Y. Y. Lin, and T. P. Kuma, "High-capacity disordered carbons derived from peanut shells as lithium-intercalating anode materials," *Synth. Met.*, vol. 139, no. 1, pp. 71–80, 2003.

[19] Y. Yishi, T. Nishida, S. Suda, and M. Kobayashi, "Anode material for high energy density rechargeable lithium-ion battery," *Hitachi Company Technical Report*, vol. 47, pp. 29–32, 2006.

[20] Y. H. Lee, K. C. Pan, Y. Y. Lin, T. P. Kumar, and G. T. Fey, "Lithium intercalation in graphites precipitated from pig iron melts," *Mater. Chem. Phys.*, vol. 82, pp. 750–757, 2003.

[21] T. P. Kumar, R. Ramesh, Y. Y. Lin, and G. T. K. Fey, "Tin-filled carbon nanotubes as insertion anode materials for lithium-ion batteries," *Electrochem. Commun.*, vol. 6, pp. 520–525, 2004.

[22] J. Chen, Y. Liu, A. I. Minett, C. Lynam, J. Wang, and G. G. Wallace, "Flexible, aligned carbon nanotube/conducting polymer electrodes for a lithium-ion battery," *Chem. Mater.*, vol. 19, pp. 3595–3597, 2007.

[23] Y. Kwon, G. S. Park, and J. Cho, "Synthesis and electrochemical properties of lithium-electroactive surface-stabilized silicon quantum dots," *Electrochim. Acta*, vol. 52, pp. 4663–4668, 2007.

[24] J.-H. Kim, H.-J. Sohn, H. Kim, G. Jeong, and W. Choi, "Enhanced cycle performance of sio-c composite anode for lithium-ion batteries," *J. Power Sources*, vol. 170, pp. 456–459, 2007.

[25] C. K. Chan, H. Peng, K. M. G. Liu and, X. F. Zhang, R. A. Huggins, and Y. Cui, "High-performance lithium battery anodes using silicon nanowires," *Nature Nanotechnology*, vol. 3, pp. 31–35, 2008.

[26] D. Aurbach, Y. Talyosef, B. Markovsky, E. Markevich, E. Zinigrad, L. Asraf, J. S. Gnanaraj, and H.-J. Kim, "Design of electrolyte solutions for li and li-ion batteries: a review," *Electrochimica Acta*, vol. 50, pp. 247–254, 2004.

[27] T. Jackson, *Lithium.* Marshall Cavendish Corporation, New York, USA, 2007.

[28] F. Galobardes, C. Wang, and M. Madou, "Investigation on the solid electrolyte interface formed on pyrolyzed photoresist carbon anodes for c-mems lithium-ion batteries," *Diamond & Related Materials*, vol. 15, pp. 1930–1934, 2006.

[29] P. Verma, P. Maire, and P. Novák, "A review of the features and analyses of the solid electrolyte interphase in li-ion batteries," *Electrochimica Acta*, vol. 55, no. 22, pp. 6332 – 6341, 2010.

[30] A. M. Andersson and K. Edström, "Chemical composition and morphology of the elevated temperature sei on graphite," *Journal of The Electrochemical Society*, vol. 148, no. 10, pp. A1100–A1109, 2001.

[31] S. S. Zhang, "Electrochemical study of the formation of a solid electrolyte interface on graphite in a libc$_2$o$_4$f$_2$-based electrolyte," *Journal of Power Sources*, vol. 163, pp. 713–718, 2007.

[32] Y. Wang, F. Su, C. D. Wood, J. Y. Lee, and X. S. Zhao, "Preparation and characterization of carbon nanospheres as anode materials in lithium-ion secondary batteries," *Ind. Eng. Chem. Res.*, vol. 47, pp. 2294–2300, 2008.

[33] H. Wang, T. Abe, S. Maruyama, Y. Iriyama, Z. Ogumi, and K. Yoshikawa, "Graphitized carbon nanobeads with an onion texture as a lithium-ion battery

negative electrode for high-rate use," *Advanced Materials*, vol. 17, p. 2857?2860, 2005.

[34] G.-C. Chung, "Reconsideration of sei stability: reversible lithium intercalation into graphite electrodes in trans-2,3-butylene carbonate," *Journal of Power Sources*, vol. 104, no. 1, pp. 7 – 12, 2002.

[35] K. Persson, V. A. Sethuraman, L. J. Hardwick, Y. Hinuma, Y. S. Meng, A. van der Ven, V. Srinivasan, R. Kostecki, and G. Ceder, "Lithium diffusion in graphitic carbon," *The Journal of Physical Chemistry Letters*, vol. 1, no. 8, pp. 1176–1180, 2010.

[36] S. Iijima, "Helical microtubules of graphitic carbon," *Nature*, vol. 354, pp. 56–58, 1991.

[37] H. W. Kroto, J. R. Heath, S. C. O'Brien, R. F. Curl, and R. E. Smalley, "C_{60}: Buckminsterfullerene," *Nature*, vol. 318, pp. 162 – 163, 1985.

[38] M. F. Yu, O. Lourie, M. J. Dyer, K. Moloni, T. F. Kelly, and R. S. Ruoff, "Strength and breaking mechanism of multiwalled carbon nanotubes under tensile load," *Science*, vol. 287, pp. 637–640, 2000.

[39] X. Lu and Z. Chen, "Curved pi-conjugation, aromaticity, and the related chemistry of small fullerenes ($< c_{60}$) and single-walled carbon nanotubes," *Chem. Rev.*, vol. 105, no. 10, pp. 3643–3696, 2005.

[40] A. Y. Ganin, Y. Takabayashi, Y. Z. Khimyak, S. Margadonna, A. Tamai, M. J. Rosseinsky, and K. Prassides, "Bulk superconductivity at 38 k in a molecular system," *Nature Materials*, vol. 7, pp. 367–371, 2008.

[41] K. S. Novoselov, A. K. Geim, S. V. Morozov, D. Jiang, Y. Zhang, S. V. Dubonos, I. V. Grigorieva, and A. A. Firsov, "Electric field effect in atomically thin carbon films," *Science*, vol. 306, pp. 666–669, 2004.

[42] "Graphene - scientific background on the nobel prize in physics 2010." by Class for Physics of the Royal Swedish Academy of Science, Stockholm, Sweden, Information retrieved 02.12.2010.

[43] J. Muller, A. T. Skjeltorp, G. Helgesen, K. D. Knudsen, and H. Heiberg-Andersen, *Silicon Versus Carbon - Fundamental Nanoprocesses, Nanobiotachnology and Risks Assessment*, ch. Carbon Discs and Carbon Cones - New High Risk Material for Nano-Sensors With Low Detection Limit and Fast Kinetics, pp. 285–292. Springer, 2009.

[44] n-TEC, http://www.n-tec.no, Information retrieved 14.12.2010.

[45] H. Heiberg-Andersen, A. T. Skjeltorp, and K. Sattler, "Carbon nanocones: A variety of non-crystalline graphite," *Journal of Non-Crystalline Solids*, vol. 354, pp. 5247–5249, 2008.

[46] N. Yang, G. Zhang, and B. Li, "Carbon nanocone: A promising thermal rectifier," *Appl. Phys. Lett.*, vol. 93, pp. 243111–1–243111–3, 2008.

[47] M. Yoo, C. W. Frank, S. Mori, and S. Yamaguchi, "Interaction of poly(vinylidene fluoride) with graphite particles. 2. effect of solvent evaporation kinetics and chemical properties of pvdf on the surface morphology of a composite film and its relation to electrochemical performance," *Chem. Mater.*, vol. 16, pp. 1945–1953, 2004.

[48] M. Yoo, C. W. Frank, and S. Mori, "Interaction of poly(vinylidene fluoride) with graphite particles. 1. surface morphology of a composite film and its relation to processing parameters," *Chem. Mater.*, vol. 15, pp. 850–861, 2003.

[49] G. Park, H. Nakamura, Y. Lee, and M. Yoshio, "The important role of additives for improved lithium ion battery safety," *J. Power Sources*, vol. 189, pp. 602–606, 2009.

[50] D. Capozzo, S. Fleming, B. Foley, and M. Macri, "Lithium ion battery safety," Master's thesis, U.S. Consumer Consumer Product Safety/Worchester Polytechnic Institute, December 2006.

[51] X. M. Wang, E. Yasukawa, and S. Kasuya, "Nonflammable trimethyl phosphate solvent-containing electrolytes for lithium-ion batteries: Ii. the use of an amorphous carbon anode," *J. Electrochem. Soc.*, vol. 148, pp. A1066–A1071, 2001.

[52] Celgard, 13800 South Lakes Dr. Charlotte, NC 28273, *Celgard Microporous Membranes, Celgard Overview Borchure, Celgard.com,*, 2010. Information retrieved 02.12.2010.

[53] E. J. Yoo, J. Kim, E. Hosono, H.-S. Zhou, T. Kudo, and I. Honma, "Large reversible li storage of graphene nanosheet families for use in rechargeable lithium ion batteries," *Nano. Let.*, vol. 8, no. 8, pp. 2277–2282, 2008.

[54] X. Wu, Z. Wang, L. Chen, and X. Huang, "Carbon/b_2o_3 composite with higher capacity for lithium storage," *Solid State Ionics*, vol. 170, pp. 117–121, 2004.

[55] F. Su, X. S. Zhao, Y. Wang, L. Wang, and J. Y. Lee, "Hollow carbon spheres with a controllable shell structure," *J. Mater. Chem.*, vol. 16, pp. 4413–4419, 2006.

[56] V. G. Khomenko and V. Z. Baruskov, “Characterization of silicon- and carbon-based composite anodes for lithium-ion batteries,” *Electrochem. Acta*, vol. 52, pp. 2829–2840, 2007.

[57] H. Günzler and H.-U. Gremlich, *IR Spectroscopy - An Introducion*. 69469 Weinheim, Germany: WILEY-VCG Verlag GmbH, 2002. ISBN 3-527-28896-1.

[58] “Michelson interferometer.” Wikipedia.org. http://en.wikipedia.org/wiki/File:Interferometer.svg, Information retrieved 02.06.2011.

[59] R. A. Friedel and G. I. Carlson, “Infrared spectra on ground carbon,” *The Journal of Physical Chemistry*, vol. 75, pp. 1149–1151, 1971.

[60] C. Moreno-Castilla, M. V. López-Ramón, and F. Carrasco-Marín, “Changes in surface chemistry of activated carbons by oxidation,” *Carbon*, vol. 38, pp. 1995–2001, 2000.

[61] F. Cataldo, G. Compagnini, G. Patané, O. Ursini, G. Angelini, P. R. Ribic, G. Margaritondo, A. Cricenti, G. Palleschi, and F. Valentini, “Graphene nanoribbons produced by the oxidative unzipping of single-wall carbon nanotubes,” *Carbon*, vol. 48, pp. 2596–2602, 2010.

[62] E. Fuente, J. A. Menéndez, M. A. Díez, D. Suárez, and M. A. Montes-Morán, “Infrared spectroscopy of carbon materials: A quantum chemical study of model compounds,” *J. Phys. Chem. B*, vol. 107, pp. 6350–6359, 2003.

[63] S. Wang, Y. Zhang, N. Abidi, and L. Cabrales, “Wettability and surface free energy of graphene films,” *Langmuir*, vol. 25, no. 18, pp. 11078–11081, 2009.

[64] D. B. Mawhinney and J. T. Y. Jr., “Ftir study of the oxidation of amorphous carbon by ozone at 300 k - direct cooh formation,” *Carbon*, vol. 39, pp. 1167–1173, 2001.

[65] G. Goncalves, P. A. A. P. Marques, C. M. Granadeiro, H. I. S. Nogueira, M. K. Singh, and J. Grácio, “Surface modification of graphene nanosheets with gold nanoparticles: The role of oxygen moieties at graphene surface on gold nucleation and growth,” *Chem. Mater.*, vol. 21, pp. 4796–4802, 2009.

[66] D. R. Dreyer, S. Park, C. W. Bielawski, and R. S. Ruoff, “The chemistry of graphene oxide,” *Chem. Soc. Rev.*, vol. 39, pp. 228–240, 2010.

[67] J. P. Rourke, P. A. Pandey, J. J. Moore, M. Bates, I. A. Kinloch, R. J. Young, and N. R. Wilson, “The real graphene oxide revealed: Stripping the oxidative debris from the graphene-like sheets,” *Angew. Chem. Int. Ed*, vol. 50, pp. 1–6, 2011.

[68] K.-C. Möller, H. J. Santnera, W. Kerna, S. Yamaguchib, J. O. Besenharda, and M. Wintera, “In situ characterization of the sei formation on graphite in the presence of a vinylene group containing film-forming electrolyte additives,” *J. Power Sources*, vol. 119-121, pp. 561–566, 2003.

[69] Y. Ein-Eli, B. Markovsky, D. Aurbach, Y. Carmeli, H. Yamin, and S. Luski, “The dependence of the performance of li-c intercalation anodes for li-ion secondary batteries on the electrolyte solution composition,” *Electrochimica Acta*, vol. 39, no. 17, pp. 2559 – 2569, 1994.

[70] D. Aurbach, B. Markovsky, A. Shechter, Y. Ein-Eli, and H. Cohen, “A comparative study of synthetic graphite and li electrodes in electrolyte solutions based on ethylene carbonate-dimethyl carbonate mixtures,” *Journal of The Electrochemical Society*, vol. 143, no. 12, pp. 3809–3820, 1996.

[71] D. Aurbach, Y. Gofer, M. Ben-Zion, and P. Aped, “The behaviour of lithium electrodes in propylene and ethylene carbonate: The major factors that influence li cycling efficiency,” *Journal of Electroanalytical Chemistry*, vol. 339, no. 1-2, pp. 451 – 471, 1992. An International Journal Devoted to all Aspects of Electrode Kinetics, Interfacial Structure, Properties of Electrolytes, Colloid and Biological Electrochemistry.

[72] D. Aurbach, B. Markovsky, I. Weissman, E. Levi, and Y. Ein-Eli, “On the correlation between surface chemistry and performance of graphite negative electrodes for li ion batteries,” *Electrochimica Acta*, vol. 45, no. 1-2, pp. 67 – 86, 1999.

[73] D. Aurbach, M. D. Levi, E. Levi, and A. Schechter, “Failure and stabilization mechanisms of graphite electrodes,” *The Journal of Physical Chemistry B*, vol. 101, no. 12, pp. 2195–2206, 1997.

[74] D. Aurbach, Y. Gofer, and J. Langzam, “The correlation between surface chemistry, surface morphology, and cycling efficiency of lithium electrodes in a few polar aprotic systems,” *Journal of The Electrochemical Society*, vol. 136, no. 11, pp. 3198–3205, 1989.

[75] K.-I. Morigaki and A. Ohta, “Analysis of the surface of lithium in organic electrolyte by atomic force microscopy, fourier transform infrared spectroscopy and scanning auger electron microscopy,” *Journal of Power Sources*, vol. 76, no. 2, pp. 159 – 166, 1998.

[76] A. Zaban and D. Aurbach, “Impedance spectroscopy of lithium and nickel electrodes in propylene carbonate solutions of different lithium salts a comparative study,” *Journal of Power Sources*, vol. 54, no. 2, pp. 289 – 295, 1995. Proceedings of the Seventh International Meeting on Lithium Batteries.

[77] G. V. Zhuang and J. P. N. Ross, “Analysis of the chemical composition of the passive film on li-ion battery anodes using attentuated total reflection infrared spectroscopy,” *Electrochemical and Solid-State Letters*, vol. 6, no. 7, pp. A136–A139, 2003.

[78] H. Yoshida, T. Fukunaga, T. Hazama, M. Terasaki, M. Mizutani, and M. Yamachi, “Degradation mechanism of alkyl carbonate solvents used in lithium-ion cells during initial charging,” *Journal of Power Sources*, vol. 68, no. 2, pp. 311 – 315, 1997. Proceedings of the Eighth International Meeting on Lithium Batteries.

[79] Y. Ein-Eli and D. Aurbach, “Identification of surface films formed on active metals and nonactive metal electrodes at low potentials in methyl formate solutions,” *Langmuir*, vol. 8, no. 7, pp. 1845–1850, 1992.

[80] “Bragg’s law.” Wikipedia.org. http://en.wikipedia.org/wiki/File:BraggPlane Diffraction.svg, Information retrieved 07.06.2011.

[81] J. William D. Callister and D. G. Rethwisch, *Materials Science and Engineering - An Introducion*. John Wiley & Sons, Inc., New York, USA, 7th ed., 2007.

[82] C. H. Hamann, A. Hamnett, and W. Vielstich, *Electrochemistry*. Wiley-VCH, 2007.

[83] “From powder to part - 4.1.3 forming,” December 2004. by Breviary Technical Ceramics, Information retrieved 11.12.2010.

[84] F. C. Tai, C. Wei, S. H. Chang, and W. S. Chen, “Raman and x-ray diffraction analysis on unburned carbon powder re?ned from ?y ash,” *Journal of Raman Spectroscopy*, vol. 41, no. 9, pp. 933–937, 2009.

[85] W. R. Smith and M. H. Polley, “The oxidation of graphitized carbon black.,” *The Journal of Physical Chemistry*, vol. 60, no. 5, pp. 689–691, 1956.

Appendix A

Complete test result figures

A.1 Charge/discharge

In section 4.5 the results of the charge/discharge are presented with only the first charge, first discharge, and the second charge. This is adequate to present the results of irreversible capacity loss and first charge capacity. The figures presented here are the complete test cycles of all the batteries.

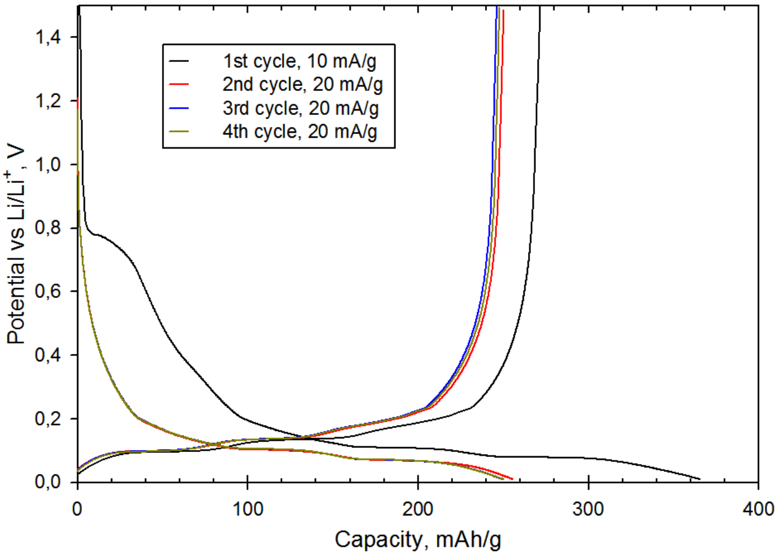

Figure A.1: Charge/discharge cycles for the HTCC2700-250μm-2.

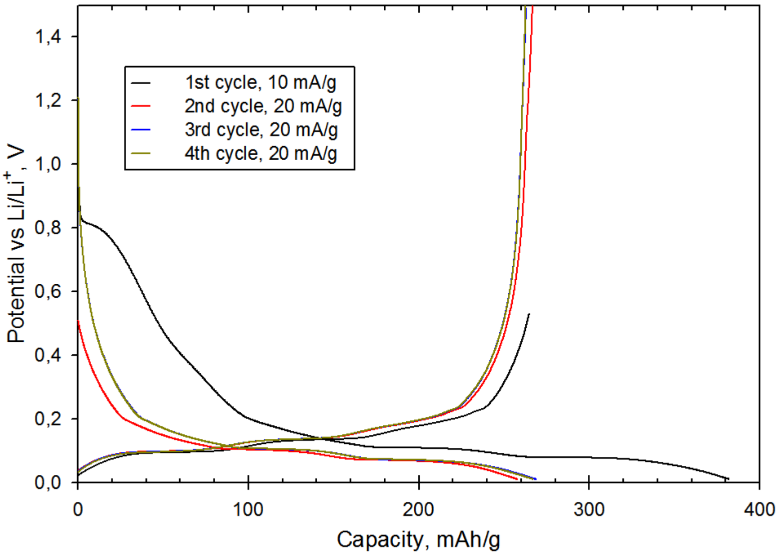

Figure A.2: Charge/discharge cycles for HTCC2700-250μm-3.

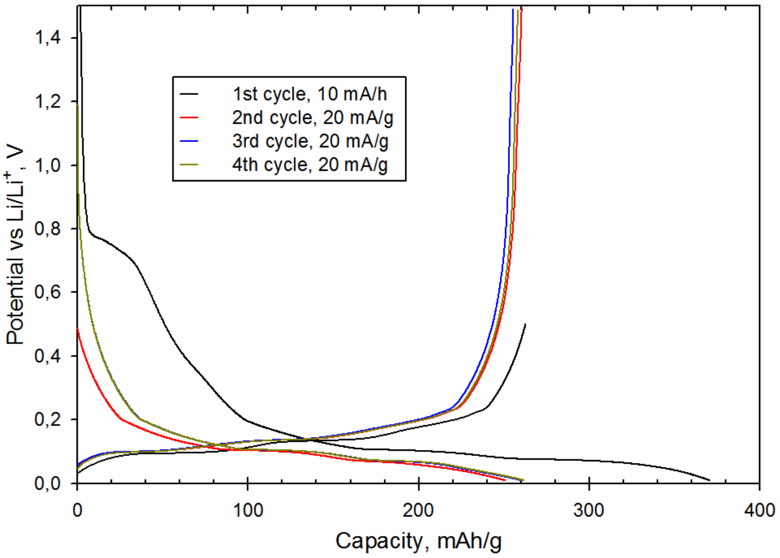

Figure A.3: Charge/discharge cycles for the HTCC2700-150μm-1.

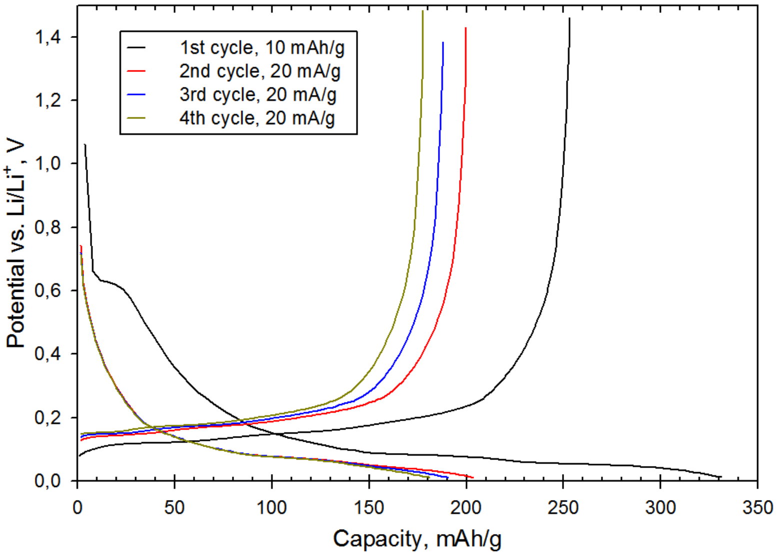

Figure A.4: Charge/discharge cycles for the HTCC2700-150μm-3.

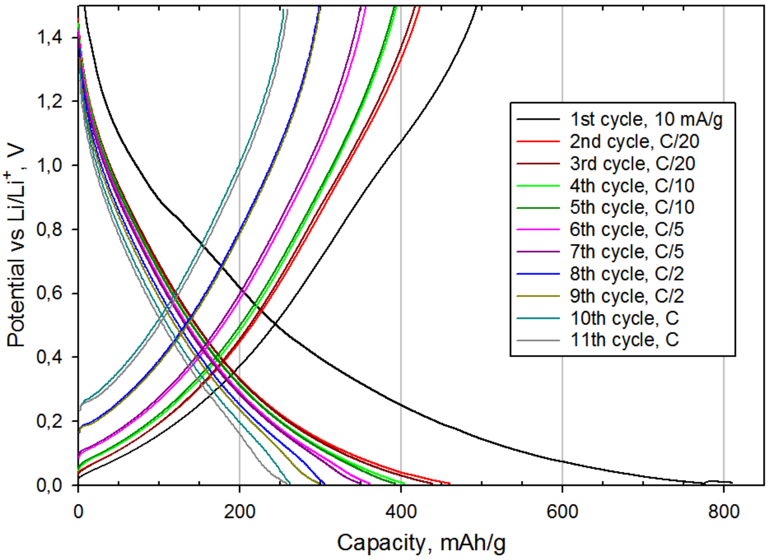

Figure A.5: Charge/discharge cycles for the CCHNO3-1.

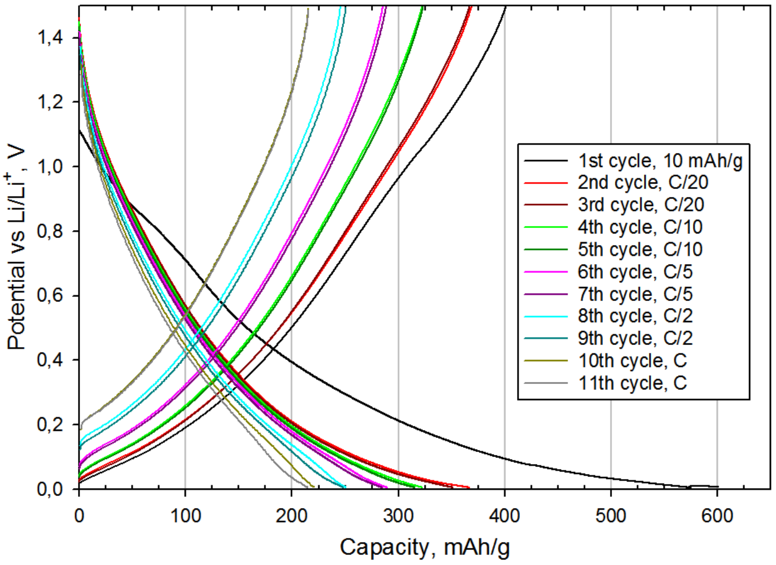

Figure A.6: Charge/discharge cycles for the CCH2O2-1.

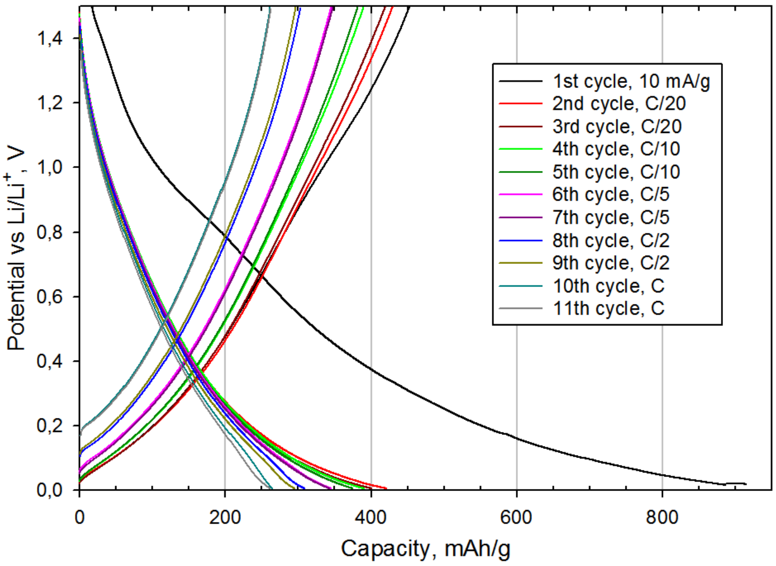

Figure A.7: Charge/discharge cycles for the CC900Air-1.

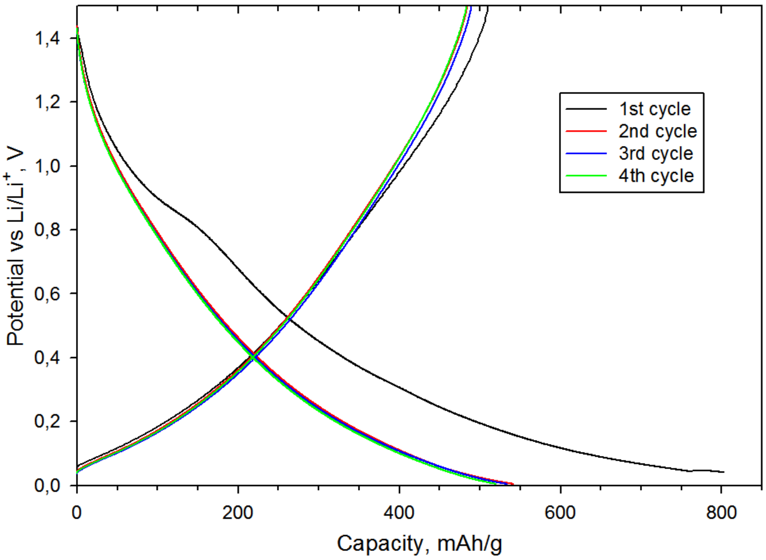

Figure A.8: Charge/discharge cycles for the HTCC950-150μm-1.

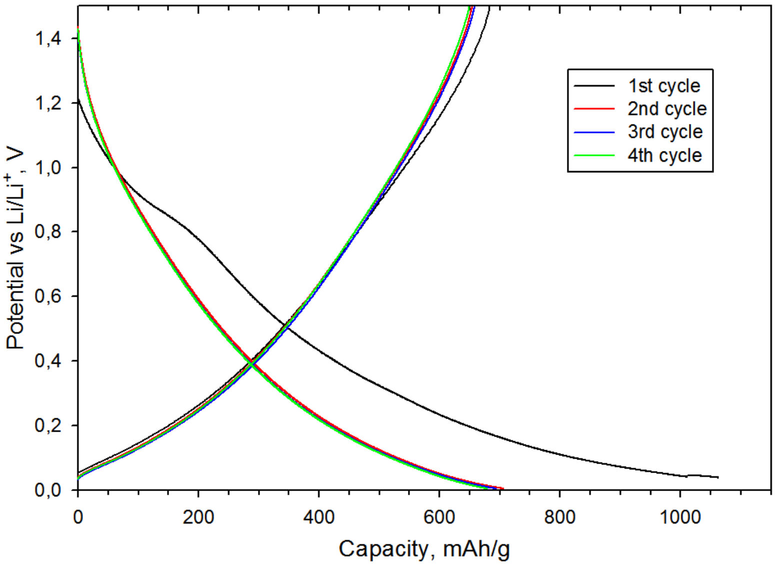

Figure A.9: Charge/discharge cycles for the HTCC950-150μm-2.

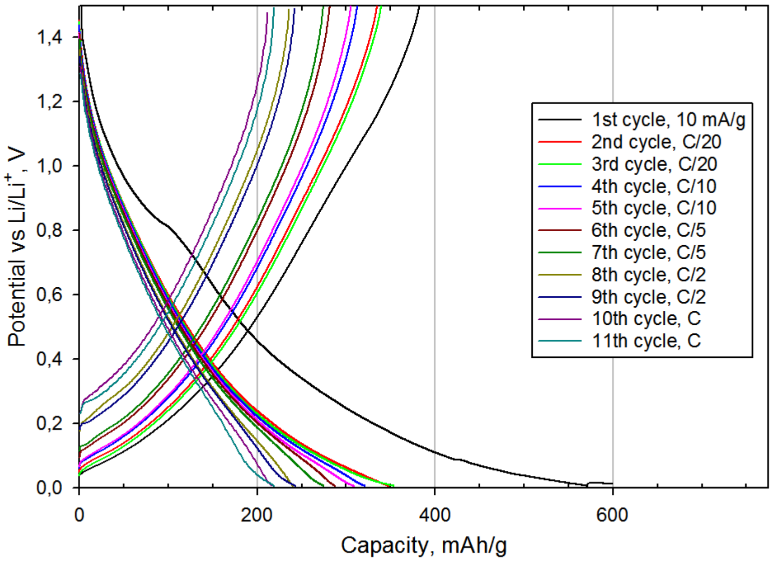

Figure A.10: Charge/discharge cycles for the HTCC950-150μm-4.

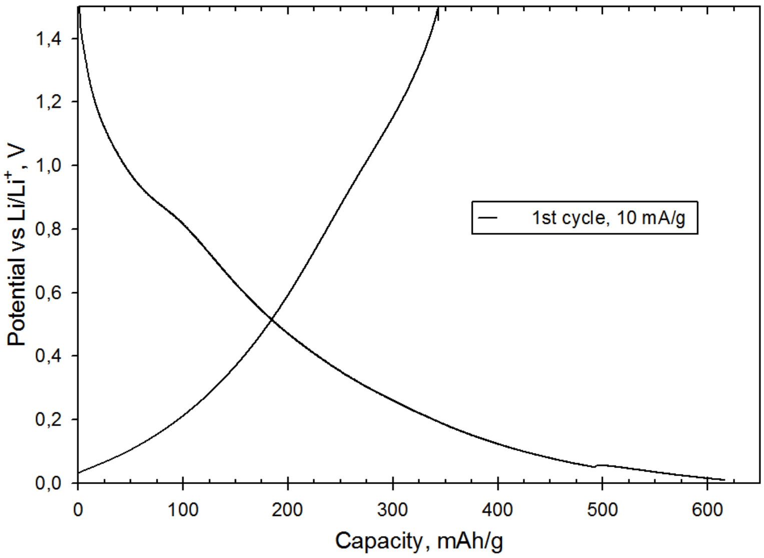

Figure A.11: Charge/discharge cycles for the MWCCAir-1.

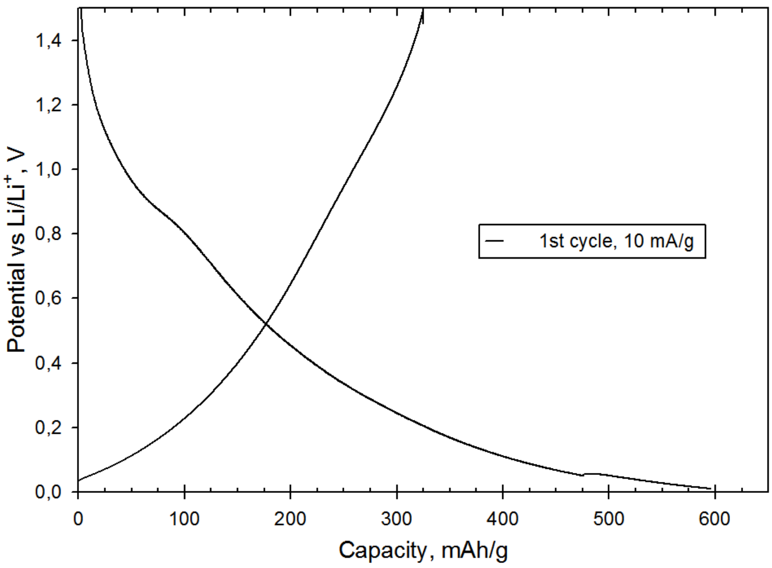

Figure A.12: Charge/discharge cycles for the MWCCAir-2.

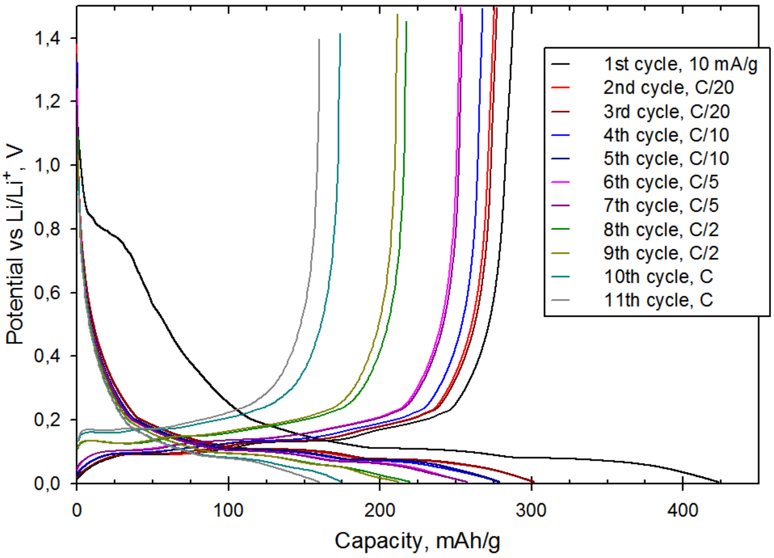

Figure A.13: Charge/discharge cycles for the CC900Air/2700-1.

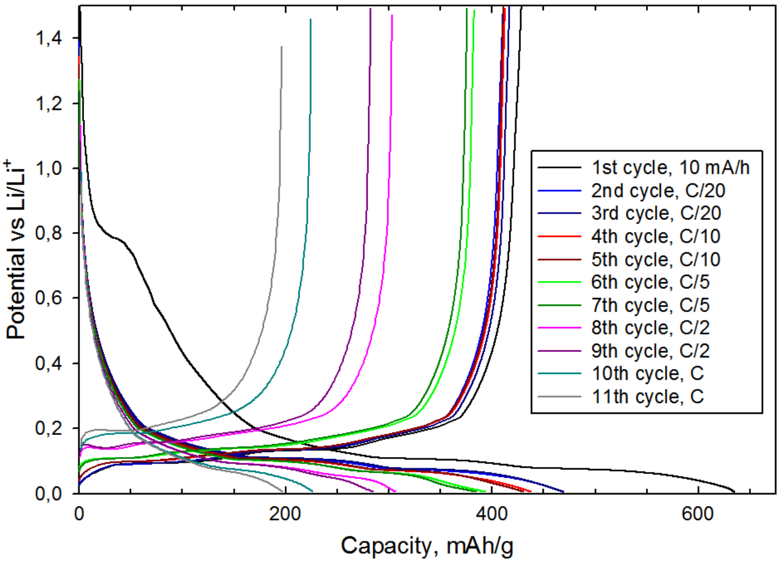

Figure A.14: Charge/discharge cycles for the CC900Air/2700-2.

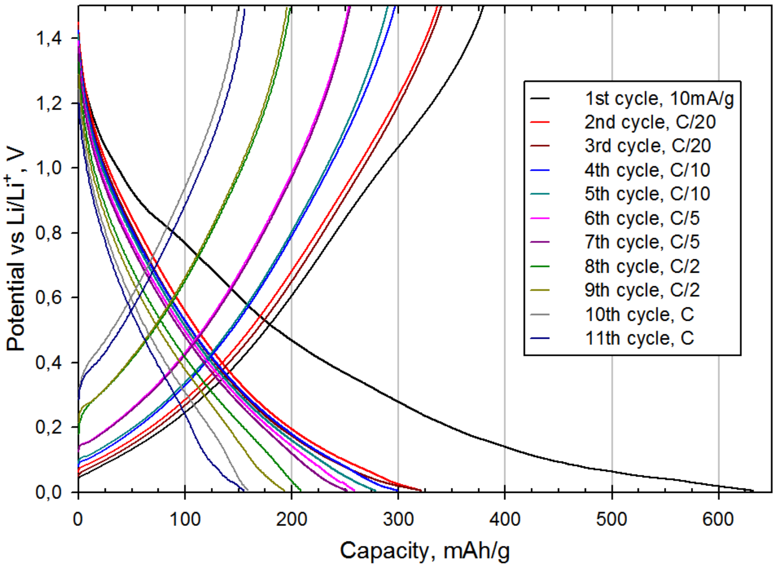

Figure A.15: Charge/discharge cycles for the CCRAW20.2-2.

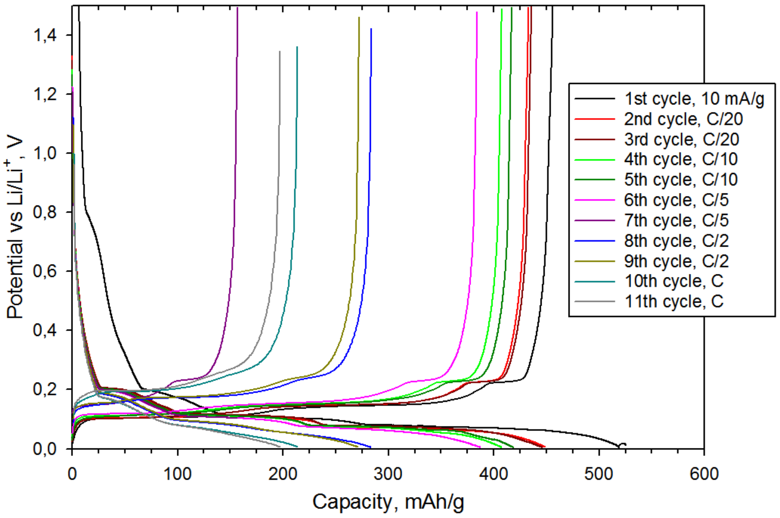

Figure A.16: Charge/discharge cycles for the SLP30-.